Coincident binding of synthetic and natural ligands to the nuclear receptor PPARγ

Jinsai Shang[1], Richard Brust[1], Sarah A. Mosure[1,2,3], Jared Bass[1], Paola Munoz-Tello[1], Hua Lin[4], Travis S. Hughes[5,6], Miru Tang[7], Qingfeng Ge[7], Theodore M. Kamenecka[4], and Douglas J. Kojetin[1,4,*]

[1]Department of Integrative Structural and Computational Biology, The Scripps Research Institute, Jupiter, Florida 33458, USA

[2]Summer Undergraduate Research Fellows (SURF) program, The Scripps Research Institute, Jupiter, Florida 33458, USA

[3]TSRI Graduate Program, The Scripps Research Institute, Jupiter, Florida 33458, USA

[4]Department of Molecular Medicine, The Scripps Research Institute, Jupiter, Florida 33458, USA

[5]Center for Biomolecular Structure and Dynamics, The University of Montana, Missoula, Montana 59812, USA

[6]Department of Biomedical and Pharmaceutical Sciences, The University of Montana, Missoula, Montana 59812, USA.

[7]Department of Chemistry and Biochemistry, Southern Illinois University, Carbondale, Illinois 62901, USA.

*Corresponding author: Douglas J. Kojetin; E-mail: dkojetin@scripps.edu

Abstract

Crystal structures of peroxisome proliferator-activated receptor gamma (PPARγ) have revealed overlapping binding modes for synthetic and natural ligands, indicating competition for the orthosteric pocket. Here we show that cobinding of a synthetic orthosteric ligand and a medium-chain fatty acid to a nonorthosteric alternate site forms a "ligand link" to the functionally important Ω-loop that synergistically affects PPARγ structure and function. Synthetic ligand extensions within the orthosteric pocket can "push" fatty acid cobinding modes towards the Ω-loop, and our retrospective analysis of the electron density of other PPARγ crystal structures bound to synthetic ligands identified alternate site density consistent with a cobound natural ligand. Mutagenesis studies indicate that residues contacting the cobound fatty acid may be important for basal cellular PPARγ activity and activation by synthetic ligands. These findings contribute to a growing body of evidence indicating ligand binding to nuclear receptors can be more complex than the classical one-for-one orthosteric exchange of natural and synthetic ligands.

Introduction

Thiazolidinediones (TZDs), also called glitazones, are synthetic agonists of the peroxisome proliferator-activated receptor gamma (PPARγ) nuclear receptor with potent anti-diabetic efficacy in patients with type 2 diabetes (1). TZDs were initially discovered in phenotypic screens of compounds with anti-diabetic efficacy (2), and later studies identified PPARγ as the molecular target (3). After an increase in clinical use of TZD drugs such as rosiglitazone (Avandia) in the early 2000s, the use of TZDs in diabetic patients has dropped significantly due to undesired side effects, including bone loss and water retention. These observations have spawned efforts to determine the mechanism by which TZDs and other synthetic PPARγ-binding ligands exert beneficial antidiabetic effects and side effects at the molecular level.

Crystal structures of the PPARγ ligand-binding domain (LBD) have been critical in determining the mechanism of action of PPARγ-binding ligands. Overall, the structure of the PPARγ LBD is described as a three-layer helical sandwich fold composed of 12 α-helices containing a dynamic or flexible internal ligand-binding pocket. The PPARγ ligand-binding pocket (***Figure 1A***) is among the largest in the nuclear receptor superfamily (4), ranging from 1200–1400 $Å^3$ in crystal structures with three branches described as "T" or "Y" shaped (5). Branch I is located proximal to helix 12, which forms a critical part of the activation function-2 (AF-2) coregulator binding surface; branch II is located near the β-sheet surface, close to the predicted

ligand entry/exit site where helix 3 meets helix 6 and the helix 11/12 loop; and branch III is also located near the β-sheet surface but deeper in the pocket near helix 5 (6-8). One of the first crystal structures of PPARγ was solved bound to the synthetic TZD ligand rosiglitazone (9), which revealed critical details on the molecular contacts formed between ligand and the binding pocket of the receptor. Subsequent crystal structures of PPARγ bound to natural ligands including medium- and long-chain fatty acids (10-14) revealed overlapping binding modes with synthetic ligands that occupy all three branches of the orthosteric pocket (5). These crystal structures and others, combined with biochemical ligand displacement assays (15-18), have revealed a competition between synthetic and natural ligands for the same orthosteric pocket.

More recent studies have shown that synthetic PPARγ ligands that bind to the orthosteric pocket can also bind to an alternate site (19-24) that partially overlaps with one of the arms of the T/Y-shaped orthosteric pocket near the β-sheet surface (branch II) but uniquely occupies space in a solvent exposed pocket formed by the flexible Ω-loop that precedes helix 3 (***Figure 1B***). Structural studies have linked ligand occupancy of branch I (i.e., the helix 12 subpocket) within the orthosteric pocket to robust stabilization of the AF-2 surface, increased "classical" transcriptional activation, and side effects associated with TZDs in part driven by hydrogen bonds formed between the TZD head group and residues within branch I (25). In contrast, ligands that either do not form hydrogen bonds in the helix 12/branch I subpocket, or bind to a combination of branch II and the alternate site, can stabilize the Ω-loop region and a nearby loop. Stabilization of this region near the Ω-loop can inhibit phosphorylation of a serine residue (Ser273 in PPARγ isoform 1 or Ser245 in isoform 2) by the Cdk5 kinase and is associated with anti-diabetic efficacy (23, 24, 26, 27).

Currently there are several PPARγ crystal structures available in the Protein Data Bank (PDB) bound to four different TZDs, including rosiglitazone, pioglitazone, rivoglitazone, and MCC-555. These ligands share a conserved ligand scaffold that occupies the branch I/helix 12 subpocket and consists of a TZD head group connected to either a phenyl moiety or a related napthyl moiety in the case of MCC-555. We were initially interested in the structural changes that allows edaglitazone (28, 29), a related TZD with a bulkier benzo[*b*]thiophene group adjacent to the TZD head group, to fit within the branch I/helix 12 subpocket. Here we solved the crystal structure of PPARγ bound to edaglitazone at the orthosteric pocket, which unexpectedly revealed a medium-chain fatty acid cobound to the alternate site. Importantly, medium-chain fatty acids activate PPAR transcription, regulate PPAR target gene expression, and influence cellular differentiation, adipogenesis, and insulin sensitization in mice indicating they are likely endogenous ligands of PPARγ (12, 30). The cobound fatty acid provides a "ligand link" to the flexible Ω-loop through a network of direct and water-mediated

hydrogen bonds, including a water-bridged hydrogen bond to edaglitazone bound to the orthosteric pocket, as well as hydrophobic and van der Waals contacts with residues in the Ω-loop. We also observed a cobound fatty acid in two new crystal structures we solved of PPARγ bound to the covalent orthosteric antagonists GW9662 and SR16832. In total, our studies—spanning crystallography, NMR spectroscopy, molecular dynamics simulations, biochemical assays and NMR studies using covalent orthosteric antagonists to block ligand binding to the orthosteric pocket, and mutagenesis coupled with cellular transcription assays—indicate that cobinding of a natural ligand to the alternate site/ Ω-loop region with a synthetic ligand at the orthosteric pocket can influence the structure and function of PPARγ.

Results

Edaglitazone is a TZD PPARγ agonist

Edaglitazone is similar in chemical structure to a commonly used PPARγ agonist rosiglitazone (***Figure 2A***), both of which possess the prototypical TZD head group. Edaglitazone has a bulkier 5-methyl-2-phenyloxazole tail group compared to the *N*-methylpyridin-2-amine tail group in rosiglitazone. Furthermore, there is a substitution of the phenyl moiety adjacent to the TZD head group in rosiglitazone for a larger benzo[*b*]thiophene moiety in edaglitazone. Edaglitazone and rosiglitazone display similar affinities for PPARγ, 141 nM and 93 nM respectively, in a fluorescent tracer ligand displacement assay (***Figure 2B***). These compounds also show similar potencies in increasing the interaction of a peptide derived from the TRAP220 coactivator (***Figure 2C***; 132 nM and 186 nM respectively), decreasing the interaction with a peptide derived from the NCoR corepressor (***Figure 2D***; 171 nM and 432 nM respectively), and in a cell-based transcriptional reporter assay (***Figure 2E***; 169 nM and 351 nM respectively).

Crystal structure of PPARγ cobound to edaglitazone and a medium-chain fatty acid

We obtained crystals of the PPARγ ligand-binding domain (LBD) by co-crystallizing protein incubated with edaglitazone. Crystals formed in the I4 space group, a different space group compared to the >150 crystal structures of PPARγ deposited in the PDB. The structure was solved at 2.1 Å (***Table 1***) as a homodimer with two molecules in the asymmetric unit (chains A and B) as an alpha helical sandwich fold. In the absence of a coregulator peptide, helix 12 typically adopts two distinct conformations in chains A and B in previously solved crystal structures—an "active" conformation, where helix 12 is docked into the AF-2 surface; and an atypical conformation via contacts to another symmetry related molecule within the unit cell. However, in our edaglitazone-bound structure, both chains adopt an active helix 12

conformation (***Figure 3A***) with nearly identical backbone conformations (Cα r.m.s.d. 0.186 Å).

Strong electron density was observed for three ligands in both chain A and B molecules (***Figure 3B, Figure S1***): one edaglitazone bound to the canonical or orthosteric pocket; a second edaglitazone to a surface pocket created through an interaction between two symmetry-related protein molecules (***Figure S2***); and a medium-chain fatty acid consistent with the size of a nonanoic acid (C9) molecule bound to a solvent accessible region near helix 3, the β-sheet surface of the orthosteric pocket, and the flexible Ω-loop region. Notably, a previous study showed that PPARγ expressed in *E. coli* can retain medium-chain fatty acids from the bacteria, predominately nonanoic acid, which function as natural PPARγ agonists (12, 30). The combined binding of the nonanoic acid and the second edaglitazone may have contributed to the stability of the PPARγ Ω-loop, which is often characterized with very poor or absent electron density in most published crystal structures.

Structural changes that accommodate the benzo[b]thiophene moiety

When bound to the orthosteric pocket, rosiglitazone (***Figure 4A***) and edaglitazone (***Figure 4B***) make conserved hydrogen bonds via the TZD head group to the side chains of Ser289 (helix 3), His323 (helix 5), His449 (helix 10/11), and Tyr473 (helix 12). The TZD head group of rosiglitazone also makes a hydrogen bond to Gln286 (helix 3), which is not present in the edaglitazone-bound structure due to a 2.8 Å shift of the Gln286 side chain from the rosiglitazone-bound position (5.7 Å away from the TZD 2-carbonyl position). This occurs due to a rearrangement of the N-terminal region of helix 3 in the edaglitazone-bound structure, which affects the conformation of Gln286 more than Ser289 (***Figure 4C***). Additional conformational changes in the edaglitazone-bound structure move helix 6 and the loop connecting helix 6–7 away from the ligand-binding pocket, and the movement of helix 3 also causes a concomitant movement of helix 12. Finally, Phe363 and Met364 are found in the loop connecting helix 6–7 with secondary structure elements classified as a hydrogen bonded turn and bend, respectively according to DSSP analysis (31). These residues undergo a shift of 6.0 Å (Phe363) and 2.6 Å (Met364) away from the ligand-binding pocket to accommodate the benzo[*b*]thiophene in the edaglitazone-bound structure, along with several other subtler changes (< 1 Å) that accommodate 5-methyl-2-phenyloxazole tail group near the β-sheet surface (***Figure 4D***).

Medium-chain fatty acids in other synthetic ligand-bound crystal structures

A previous study reported a crystal structure of PPARγ LBD that was obtained using protein purified from *E. coli*, which revealed the presence of endogenous bacterial

medium-chain fatty acids (30). Specifically, three molecules of nonanoic acid were observed in the orthosteric pocket (***Figure 5A***) in overlapping space where edaglitazone is bound in our structure (***Figure 5B***). In our edaglitazone-bound crystal structure there is clear density for a medium-chain fatty acid near helix 3, the β-sheet surface of the orthosteric pocket, and the flexible Ω-loop region. This region is referred to as an "alternate" or "allosteric" site, because other studies have shown that synthetic ligands that have crystallized in the orthosteric pocket can also bind to this alternate site. Alternate site binding occurs via a second molar equivalent of ligand, i.e. one bound to the orthosteric pocket and a second to the alternate site (19-21); when the orthosteric pocket is blocked by a covalent antagonist inhibitor that physically blocks the orthosteric pocket (19, 21, 23, 24); or via one equivalent through an alternate binding mode (23, 24).

We wondered whether there could be density present for a medium-chain fatty acid in previously published crystal structures of PPARγ bound to synthetic ligands, which may not have been modeled during structure determination because it could have been unexpected at the time. Analysis of the electron density maps deposited to the PDB for two relatively high resolution (~2 Å) crystal structures bound to rosiglitazone (PDB code 1FM6) and MCC-555 (PDB code 3B0Q) revealed extra unidentified densities suggesting there could be a medium-chain fatty acid bound in a similar manner to what we observed in the edaglitazone structure. In a crystal structure of RXRα-PPARγ LBD heterodimer where PPARγ was bound to rosiglitazone (PDB code 1FM6) solved to 2.1 Å (32), two water molecules were modeled next to rosiglitazone where the nonanoic acid is bound in our edaglitazone structure (***Figure 5C***). We found that replacement of the water molecules with a nonanoic acid better describes the density in this region (***Figure 5D***). In a crystal structure of PPARγ bound to MCC-555 (PDB code 3B0Q) solved to 2.1 Å, we also found unmodeled density (***Figure 5E***) consistent with a medium-chain fatty acid present in the same region (***Figure 5F***). Additionally, we found density consistent with a medium-chain fatty acid in crystal structures of PPARγ bound to GQ-16 (***Figure 5G***) and SR145 (***Figure 5H***), which had been solved to 2.1 Å and 2.2 Å, respectively (33, 34). These observations suggest that cobound medium-chain fatty acids may be present in other synthetic ligand-bound PPARγ crystal structures.

NMR validates cobinding of nonanoic acid with rosiglitazone and edaglitazone

The aforementioned crystal structures indicate that fatty acids present in bacteria such as nonanoic acid can remain bound to PPARγ during purification. To verify this, we performed differential 2D [^{1}H,^{15}N]-TROSY HSQC NMR analysis, which revealed subtle chemical shift and peak intensity/line broadening changes when comparing data

of ^{15}N-labeled PPARγ LBD subjected to a delipidation protocol and "native" protein that was not subjected to delipidation (***Figure S3***). Notably, titration of nonanoic acid into native PPARγ caused additional selective NMR chemical shift changes (***Figure S4***), indicating that native protein is likely partially bound to a bacterial fatty acid. We have observed that, compared to delipidated proteins, native NMR chemical shift changes are batch dependent. Native PPARγ NMR spectra can also appear nearly identical to delipidated PPARγ NMR spectra, indicating that the amount of bacterial lipid that may be bound and retained during purification can vary from substoichiometric to almost none. These changes can result from how the protein purification is performed, such as the length of chromatography or dialysis steps, or variability of fatty acid content depending on the bacterial growth media used, as the use of minimal vs. rich media can change exogenous fatty acid content within bacteria (35).

We performed differential NMR analysis of rosiglitazone-bound forms of native and delipidated PPARγ to determine if there could be cobinding of a synthetic TZD to native protein bound substoichiometrically to a fatty acid. Although the NMR spectra overlay very closely (***Figure S5***), subtle NMR chemical shift perturbations were observed for a select number of peaks (***Figure 6A***), including residues in our crystal structure near the nonanoic acid bound to the alternate site on helix 3 (Val277, Gln283, and Gly284), as well as residues within the AF-2 surface on helix 5 (Leu317 and Lys319) and helix 12 (Leu465, Ile472, and Lys474). Furthermore, several NMR peaks with weak intensities in the native form showed narrower, more intense peaks in the delipidated form (***Figure 6A***; "new" label). In our previous NMR analysis of rosiglitazone-bound PPARγ (36), we were unable to assign these peaks due to their weak and/or absent peaks in 3D NMR data, likely due to the substoichiometric cobinding of a fatty acid.

To further confirm fatty acid cobinding, we titrated nonanoic acid into rosiglitazone-bound native PPARγ (***Figure 6B, Figure S6***) and delipidated PPARγ (***Figure 6C, Figure S7***) and again performed differential NMR analysis. The binding affinity of nonanoic acid (***Figure S8***) is ~50,000-fold weaker than rosiglitazone; thus, to eliminate competition for the orthosteric pocket, we titrated one and three molar equivalents of nonanoic acid into PPARγ pretreated with two molar equivalents of rosiglitazone. This analysis again revealed subtle NMR chemical shift perturbations for essentially the same residues that were affected in the differential analysis of rosiglitazone bound to native or delipidated forms without added nonanoic acid (***Figure 6A***). Notably, the direction of the chemical shift change that occurs upon titration of nonanoic acid to rosiglitazone-bound native (***Figure 6B***) or delipidated (***Figure 6C***) PPARγ is the same direction of the shift that occurs when comparing rosiglitazone-bound native and delipidated PPARγ without added nonanoic acid (***Figure 6A***). In fact, the peak position of rosiglitazone-bound native PPARγ shows a "head start" in shifting

compared to delipidated PPARγ, which further supports that native rosiglitazone-bound PPARγ is substoichiometrically bound to a medium-chain fatty acid. In agreement with our edaglitazone cobound crystal structure, nonanoic acid cobinding effects were similarly observed in differential NMR analysis of edaglitazone-bound PPARγ (***Figure 6C, Figure S9***).

If nonanoic acid was competing with rosiglitazone bound to the orthosteric pocket, residues near the TZD head group such as His323, which forms a side chain-mediated hydrogen bond with the aromatic TZD head group, would likely shift significantly. Aromatic ring current effects, which have a significant influence on NMR peak positions, would change in this portion of the orthosteric pocket if nonanoic acid displaced rosiglitazone. However, only very minor shifting is observed for the His323 NMR peak as compared to the larger shifting that occurs for residues near the bound nonanoic acid in our crystal structure (***Figure 6B,C***). Furthermore, other NMR peaks affected by nonanoic binding to PPARγ in the absence of rosiglitazone are not affected in the cobinding experiments with rosiglitazone, nor do they move from the rosiglitazone-bound peak position to the nonanoic acid-bound peak position (***Figure S10***). These observations support the cobinding of nonanoic, not orthosteric competition of nonanoic acid, under our experimental conditions.

Molecular simulations reveal conformational effects afforded by ligand cobinding

Our NMR results indicate that fatty acid cobinding to the alternate site when a TZD is bound to the orthosteric pocket can affect the conformation of the AF-2 surface. We performed molecular simulations to determine the potential conformational consequences of the cobinding of edaglitazone and nonanoic acid. Two microsecond simulations were conducted with edaglitazone bound to the orthosteric pocket in the absence or presence of nonanoic acid at the alternate site. For each ligand-bound state, two replicate simulations on the chain A and B crystallized conformations were performed resulting in a total of eight stable simulations (***Figure 7A***) allowing averaging of up to four simulations for each state. In all eight simulations, edaglitazone remained stably bound to the orthosteric pocket (***Figure 7B***). Nonanoic acid remained stably bound to the alternate site in three out of four simulations with edaglitazone cobound to the orthosteric pocket (***Figure 7C***). The simulation where nonanoic acid exchanged out of the alternate site was therefore excluded from a comparative analysis.

The conformation of the Ω-loop has been shown to be important in regulating the conformation of helix 12, a critical structural element in the AF-2 surface (13, 14, 37, 38). Conformational fluctuations in the Ω-loop when bound to edaglitazone alone, calculated as the coordinate R.M.S.D. relative to the crystallized conformation after minimization and equilibration, range between 4–6 Å (***Figure 7D***). However, when

cobound to nonanoic acid, Ω-loop conformational fluctuations show a broader range of smaller R.M.S.D. values (2–5 Å) with a notable increase in the 2–4 Å range relative to edaglitazone bound alone. Thus, a conformational stabilizing effect is observed for Ω-loop residues that contact the bound nonanoic acid. The loop connecting helix 1 and helix 2a, which is proximal to the Ω-loop and contains a residue (Ser245 in PPARγ1; Ser273 in PPARγ2) that is phosphorylated by the kinase Cdk5 (25), also shows reduced conformational fluctuation when cobound to nonanoic acid relative to edaglitazone bound alone (***Figure 7E***). NMR analysis reveals that nonanoic acid cobinding with rosiglitazone or edaglitazone affects the conformation of residues near Ser245/Ser273 (***Figure S11***). These observations support studies showing that ligand occupancy of the alternate site can affect the conformation of this surface and inhibit Cdk5-mediated phosphorylation of Ser245 (24). Finally, nonanoic acid cobinding to the alternate site stabilizes the conformation of helix 12, which shows decreased R.M.S.D. values relative to edaglitazone bound alone (***Figure 7F***). This is consistent with our NMR data (***Figure 6***) showing that cobinding of nonanoic acid with rosiglitazone or edaglitazone affects NMR peaks for residues within the helix 12/AF-2 surface.

Structural validation of fatty acid cobinding with covalent orthosteric antagonists

We sought to validate our crystal structure showing cobinding of edaglitazone and nonanoic acid by performing TR-FRET biochemical assays where we titrated nonanoic acid into PPARγ with a saturating concentration of TZD (edaglitazone or rosiglitazone), which causes the TR-FRET assay window to reach maximal values because the protein reaches a high affinity/fully peptide-bound state (**Figure 2C**). Titration of nonanoic acid in the presence of edaglitazone or rosiglitazone showed a slight decrease in TRAP220 coactivator binding and increase in NCoR corepressor binding (***Figure 8A***). However, in these experiments it is difficult to differentiate between nonanoic acid cobinding with a TZD and ligand competition (i.e., nonanoic acid competing with rosiglitazone for the orthosteric pocket). Because of these challenges, we performed TR-FRET assays in the absence and presence of covalent antagonists GW9662, T0070907, and SR16832 (***Figure S12***) that covalently bind to Cys285 located in, and block ligand binding to, the orthosteric pocket (22, 39, 40).

Structural superposition of an available crystal structure of GW9662-bound PPARγ (PDB code 3B0R) with a crystal structure of PPARγ bound to nonanoic acid (30) (PDB code 4EMA) revealed that GW9662 overlaps with two out of the three crystallized nonanoic acid binding modes in braches I and III (***Figure 8B***). We also solved crystal structures of PPARγ bound to GW9662 and SR16832 (22), an analog of GW9662 with a ligand extension towards the alternate site, at 2.29 Å and 2.73 Å, respectively (**Table 2**). Similar to our edaglitazone crystal structure, we observed electron density consistent

with a medium-chain fatty acid in both structures, which we modeled as nonanoic acid. In chain A of our GW9662 structure, one nonanoic acid is present within the branch II region of the orthosteric pocket; in chain B, there are two nonanoic acid molecules present, one in branch II and another closer to the cobound position in our edaglitazone structure (***Figure 8C***). In the SR16832 structure, nonanoic acid is present only in chain A; and the 6-methoxyquinoline group extension in SR16832, relative to GW9662, appears to have blocked the branch II nonanoic acid binding mode, pushing the nonanoic acid closer to the cobound position in our edaglitazone structure (***Figure 8D***).

We performed differential NMR to confirm the nonanoic acid binding regions in the crystal structures of PPARγ bound to GW9662 and SR16832. The analysis was limited relative to the analysis we performed above for rosiglitazone and edaglitazone because about half of the expected NMR peaks are missing due to intermediate exchange on the NMR time scale from significant μs–ms time scale dynamics present when bound to covalent antagonists relative to agonists that robustly stabilize the dynamics of PPARγ (19, 21, 22, 36, 41). Despite this limitation, chemical shift perturbations were observed for residues near the crystallized nonanoic acid binding modes observed in the GW9662 and SR16832 crystal structures (***Figure 8E and F, respectively***), including residues on helix 2b/β-sheet surface such as Ile249, Leu255, Gly258, Leu340, Gly344, Gly346, and Phe347, confirming the crystallized nonanoic acid binding modes.

Using a TR-FRET biochemical assay, we tested the ability of nonanoic acid to increase binding of the TRAP220 coactivator peptide in the absence or presence of GW9662, T0070907, and SR16832 (***Figure 8G, Figure S12, Figure S13***). GW9662 and T0070907, which have similar structural sizes, weakened the potency of nonanoic acid relative to apo-PPARγ (i.e., lacking an orthosteric covalent antagonist). This may be due to a reduction in orthosteric binding mode contacts, including a nonanoic acid molecule that forms hydrogen bonds to the side chains of residues Ser289, His323, His449, and Tyr473 similar to the TZD head group in the nonanoic acid-bound crystal structure (30). In contrast, nonanoic acid was more potent in the presence of SR16832, which has a larger size than GW9662 and T0070907 that points towards and blocks the branch II nonanoic acid binding mode. Inspection of the SR16832 crystal structure cobound to nonanoic acid indicates the increased potency is likely due to hydrogen bonds between the aryl ether/methoxy group of SR16832 with the carboxylate head group and other aliphatic protons in nonanoic acid (***Figure S14***), the latter of which can form weak hydrogen bonds with methoxy groups (42). In support of this hydrogen bond network, density functional theory calculations revealed a net attractive interaction between nonanoic acid and the SR16832 methoxy group (10.3 kcal/mol) and a repulsive interaction with the phenyl moiety of GW9662 (8.56 kcal/mol). We similarly observed

binding for decanoic acid (C10) and dodecanoic acid (C12) in the presence of GW9662, although SR16832 is more effective at blocking these larger medium-chain fatty acids (***Figure S15***).

Mutation of nonanoic acid hydrogen bond contacts decreases PPARγ cellular activation

We analyzed the hydrogen bond network in the molecular simulations to establish the binding determinants of nonanoic acid cobinding with edaglitazone. Several hydrogen bonds between the carboxylate head group of nonanoic acid and various backbone and side chain groups of PPARγ were observed in all three simulations (***Figure 9A***), and among these the hydrogen bonds to the Lys265 backbone and Ser342 side chain were also observed in the crystal structure. The hydrogen bond to the His266 backbone observed in the crystal structure was lowly populated in the simulation, and new hydrogen bonds were detected with the Arg288 side chain. Notably, a complex network of water-bridged hydrogen bonds was observed (***Figure 9B***), including several different types of water-mediated hydrogen bonds linking the oxazole nitrogen atom in edaglitazone to the carboxylate head group of nonanoic acid (***Figure 9C***). In addition to these hydrogen bonds, a network of hydrophobic interactions was observed in all three simulations (***Figure 9D***), including the side chains of Leu255, Phe264, Val277, Arg280, Ile281, Phe287, and the terminal phenyl group of edaglitazone interacts with the saturated carbon side chain of nonanoic acid (***Figure 9E***).

To determine the functional importance of residues that hydrogen bond to nonanoic acid, we tested individual and grouped alanine mutants for Lys265, Arg288, and Ser342 in a cell-based transcriptional reporter assay. All of the mutants lowered the basal transcriptional activity of PPARγ in the DMSO control treated condition (***Figure 10A***) without affecting PPARγ protein levels in cells (***Figure S16***). This indicates the residues are important for mediating the functional activity of PPARγ when bound to natural ligands within cells. Furthermore, the mutants showed reduced activity at saturating synthetic ligand concentrations (***Figure 10A,B***) without affecting the potency of the synthetic ligands (***Figure 10B***). This indicates that the mutations also reduce the activation synergy between synthetic ligands and natural ligands present within cells because the activity in the presence of the synthetic ligand is lower for the mutants compared to wild-type PPARγ. We used TR-FRET biochemical assays to determine if nonanoic acid potency for affecting the interaction with the TRAP220 coactivator peptide, used as a proxy for binding affinity, is affected by the individual alanine mutations. The mutants alone did not show a significant change on coregulatory affinity (***Figure S17***), nor they cause a significant change in potency both in the absence or presence of GW9662 to better isolate alternate site binding of nonanoic acid (***Figure S18***). Similarly, alanine mutation of RXRα Arg316, which forms a side chain-mediated

hydrogen bond to the carboxylate head group of docosahexaenoic Ω-loop acid (43), does not affect ligand binding (***Figure S10***). Taken together, this indicates the residues that formed hydrogen bonds with nonanoic acid in the alternate site may be important for mediating the basal cellular activity of PPARγ and activation by TZDs; however, hydrophobic interactions and perhaps compensating hydrogen bonds mediated by backbone atoms or the complicated network of water-mediated hydrogen bonds may all contribute to nonanoic acid binding.

Discussion

Synthetic ligands and FDA-approved anti-diabetic drugs that target the nuclear receptor PPARγ have been shown to compete with natural ligands in binding to an orthosteric pocket to regulate PPARγ activity. Here, we present a crystal structure of PPARγ bound to the TZD edaglitazone, which also revealed a medium-chain fatty acid, which copurified with PPARγ protein expressed in bacteria, bound at an alternate site—a region known to be important in regulating PPARγ structure and function (13, 14, 23, 24, 37, 38). We validated the cobinding of nonanoic acid with edaglitazone and rosiglitazone using NMR spectroscopy. NMR chemical shift perturbations were observed not only at the alternate site but also in the AF-2 surface, revealing a structural synergy in cobinding of natural and synthetic ligands that affects the coregulator interaction surface. Furthermore, using covalent antagonists as chemical tools to block binding of nonanoic acid to the orthosteric pocket, we confirmed alternate site binding of nonanoic acid, showed that orthosteric ligand extensions that occupy a larger region of the orthosteric pocket can push nonanoic acid binding modes towards the Ω-loop, and that alternate site binding of nonanoic acid can affect coregulator recruitment in the TR-FRET assay. Our molecular simulation studies also confirm that nonanoic acid remains stably cobound to the alternate site with edaglitazone bound to the orthosteric pocket. The simulation data show that alternate site cobinding of nonanoic acid and edaglitazone not only stabilizes the Ω-loop but it also affects the conformation of the AF-2 surface in the simulations, a finding that is supported by NMR data where the AF-2 surface is affected by cobinding of nonanoic acid.

Past structural analyses of the Ω-loop from PPARγ crystal structures have been limited. Among more than 150 crystal structures of PPARγ deposited to the PDB, only a small subset shows visible electron density for the Ω-loop. Within these structures, the Ω-loop conformation can vary considerably indicating substantial plasticity, potentially allowing this region to adapt based on the specific ligand(s) bound. In contrast to the TZD head group, which for example is responsible for forming the hydrogen bond network in branch I of the orthosteric pocket that stabilizes the conformation of helix 12, the extended TZD tail groups interact with the β-sheet/branch II portion of the

orthosteric pocket and the alternate site/Ω-loop region through hydrophobic and van der Waals contacts (5). Cobinding of a natural ligand to the alternate site with a TZD or another type of synthetic ligand at the orthosteric pocket can provide a structural means to bridge or extend the "reach" of the bound synthetic ligand to the Ω-loop.

Ligand cobinding has been observed in several other structural studies of PPARγ. For example, serotonin and fatty acid metabolites were shown to synergistically bind to different arms of the T/Y-shaped orthosteric pocket (38). Furthermore, crystal structures of PPARγ bound to fatty acids have shown the presence of one, two, or three natural ligands bound to various arms of the orthosteric pocket (10, 30). In other nuclear receptor studies, one focused on RAR-related orphan receptor gamma (RORγ) revealed cobinding of a synthetic ligand to a region similar to the branch 1/helix 12 orthosteric subpocket with the natural ligand cholesterol to the orthosteric pocket (44), while another focused on pregnane X receptor (PXR) revealed cobinding of a pharmaceutical oestrogen and an organochlorine pesticide (45). We previously showed by ^{19}F NMR spectroscopy that a synthetic ligand can bind to the alternate site when PPARγ is covalently bound to an oxidized fatty acid in the orthosteric pocket (21). Furthermore, a crystal structure of PPARγ also showed that a natural product, luteolin, can bind to the alternate site with a 14-carbon fatty acid, myristic acid, bound to the orthosteric pocket (37). Molecular simulations showed that luteolin binding stabilizes the Ω-loop and Ser245 (Ser273 in isoform 2 numbering) loop and the cobinding of luteolin and myristic acid is mediated in part through a water bridged hydrogen bond, similar to our simulations with nonanoic acid bound to the alternate site. However, to the best of our knowledge, no studies thus far have shown that a synthetic ligand bound to the orthosteric pocket can cobind with a natural ligand to the alternate site. However, our retrospective analysis of other ligand-bound PPARγ crystal structures indicate the likely presence of a medium-chain fatty acid in the alternate site where water molecules, for example, were instead modeled into the structure. While it is possible that a more comprehensive analysis of previous PPARγ crystal structures could reveal more similar situations, going forward our study should have an impact on the interpretation of future crystal structures of PPARγ and other nuclear receptors to consider possible natural and synthetic ligand cobinding scenarios, particularly if the protein was not delipidated.

Our study highlights an important but perhaps underappreciated concept of considering cobinding of natural ligands with designed synthetic ligands in drug discovery efforts. Although edaglitazone does not directly interact with the functionally important Ω-loop, nonanoic acid bound to the alternate site bridges edaglitazone to the Ω-loop and affects the conformation of several important functional surfaces. Furthermore, the water-mediated hydrogen bond network that links the edaglitazone

444 and nonanoic acid to PPARγ highlights the importance of considering solvent-mediated
445 interactions, both in the binding of a designed synthetic ligand and potential bridging
446 interactions with natural ligands. The network includes water-mediated hydrogen
447 bonds between the oxazole nitrogen atom in edaglitazone and the carboxylic acid group
448 of nonanoic acid; a significantly populated tripartite interaction between these ligand
449 atoms and the Ser342 side chain; and a quadripartite interaction that also involves the
450 Arg288 side chain. For example, pyridyl groups in the ligand scaffolds of rosiglitazone
451 and pioglitazone, which are present in the same structural region as the oxazole group
452 in edaglitazone, may afford a similar water-mediated hydrogen bond that could
453 connect these ligands to the Ω-loop as well. Furthermore, our crystal structures of
454 PPARγ bound by the covalent antagonists GW9662 and SR16832 demonstrate that fatty
455 acid cobinding modes can adapt to structural differences in the ligand scaffold bound to
456 the orthosteric pocket. This shows that solvent-mediated bridging interactions can
457 occur not only between a single ligand and its target, but also between two (or more)
458 bound ligands and the target.

459 Medium-chain fatty acids, which are not only found in bacteria but also dietarily
460 consumed by humans (46), are thought to be putative physiologically relevant ligands
461 for PPARγ due to their relatively high serum concentrations (μM–mM) and their ability
462 to modulate adipogenesis and insulin sensitization (12, 30, 47). Alanine mutations of
463 Lys265, Arg288, and Ser342 that we designed to disrupt hydrogen bonds with nonanoic
464 acid showed reduced cellular activity both in terms of basal activation and at saturating
465 synthetic TZD concentrations without affecting TZD potency or coregulator affinty.
466 This indicates these residues are important both for mediating the activity of PPARγ
467 bound to endogenous cellular ligands as well as in the activation synergy of
468 endogenous ligands cobound with a synthetic ligand (i.e. overall functional efficacy).
469 Taken together, these findings indicate that cobinding of natural ligands with a bound
470 orthosteric synthetic ligand may contribute to the activation of PPARγ imparted by
471 synthetic ligands. Although the mutations did not reduce the nonanoic acid potency in
472 the TR-FRET biochemical assay, it is possible that the mutants could affect the potency
473 or affinity of different natural ligands (i.e., a ligand other than nonanoic acid) present
474 within cells, which could also account for the lower cellular transcriptional activity of
475 the mutants. For example, we previously showed that the long chain unsaturated fatty
476 acid docosahexaenoic acid (DHA), an endogenous PPARγ ligand (48) that binds to the
477 orthosteric pocket (49), can still bind PPARγ when the orthosteric pocket is blocked by a
478 covalent antagonist (22). It is also possible that cobinding of synthetic ligands to
479 different types of natural ligands could contribute to the complex pharmacological
480 properties of synthetic nuclear receptor ligands, such as ligands that activate
481 transcription in some cell/tissue types and antagonize transcription in others; or ligands
482 that cause graded or different activation properties in different cell and tissue types.

483 Taken together, our findings indicate that the classical nuclear receptor ligand exchange
484 model, where a synthetic ligand displaces one or more natural ligands from the
485 orthosteric pocket, may be more complex than currently appreciated.

486 **Methods**

487 *Materials and reagents*

488 Rosiglitazone, edaglitazone, GW9662, and T0070907 ligands were obtained from
489 commercial sources (Cayman and Tocris Bioscience). SR16832 was synthesized in-house
490 as previously described (22). Peptides of LXXLL-containing motifs from TRAP220
491 (residues 638–656; NTKNHPMLMNLLKDNPAQD) and NCoR (2256–2278;
492 DPASNLGLEDIIRKALMGSFDDK) containing a N-terminal FITC label with a six-
493 carbon linker (Ahx) and an amidated C-terminus for stability were synthesized by
494 LifeTein.

495 *Protein purification*

496 Human PPARγ LBD (residues 203–477, isoform 1 numbering; or residues 231–
497 505, isoform 2 numbering) and human RXRα LBD (residues 223–462) were expressed in
498 *E. coli* BL21(DE3) cells using autoinduction ZY media or M9 minimal media
499 supplemented with NMR isotopes as a Tobacco Etch Virus (TEV)-cleavable N-terminal
500 hexahistidine(6xHis)-tagged fusion protein using a pET46 Ek/LIC vector (Novagen) and
501 purified using nickel affinity chromatography and size exclusion chromatography. The
502 purified proteins were concentrated to 10 mg/mL in a buffer consisting of 20 mM
503 potassium phosphate (pH 7.4), 50 mM potassium chloride, 5 mM tris(2-
504 carboxyethyl)phosphine (TCEP), and 0.5 mM ethylenediaminetetraacetic acid (EDTA).
505 Purified protein was verified by SDS-PAGE as >95% pure. For studies using a covalent
506 orthosteric antagonist, PPARγ LBD protein was incubated with at least a ~1.05x excess
507 of GW9662, T0070907, or SR16832 at 4 °C for 24 h to ensure covalent modification to
508 Cys285, then buffer exchanged the sample to remove excess covalent antagonist and
509 DMSO. Complete attachment of the covalent antagonist occurs within 30–60 minutes, as
510 detected using ESI-MS with a LTQ XL linear Ion trap mass spectrometer
511 (Thermo Scientific). For studies using delipidated protein, two protocols were used
512 (LIPIDEX and refolding) that gave similar results. For LIPDEX delipidation, protein was
513 incubated with LIPIDEX-1000 (Perkin Elmer) at 37 °C for 1h and buffer exchanged into
514 the aforementioned phosphate buffer. For delipidation by refolding, protein was first
515 subjected to a chloroform/methanol lipid extraction (50) and the denatured protein was
516 refolded using a fast dilution/dialysis procedure followed by size exclusion

517 chromatography (51). NMR spectra of delipidated protein obtained from both
518 procedures were essentially identical.

519 *TR-FRET ligand displacement and coregulator interaction assays*

520 The time-resolved fluorescence resonance energy transfer (TR-FRET) assays were
521 performed in black low-volume 384-well plates (Greiner). For the ligand displacement
522 assay, each well contained 1 nM delipidated 6xHis-PPARγ LBD protein, 1 nM
523 LanthaScreen Elite Tb-anti-HIS Antibody (Thermo Fisher Scientific), and 5 nM
524 Fluormone Pan-PPAR Green (Invitrogen) in TR-FRET buffer containing 20 mM
525 potassium phosphate (pH 8), 50 mM potassium chloride, 5 mM TCEP, and 0.005%
526 Tween-20 in the absence or presence of ligand in triplicate at a concentration equal to
527 the highest protein concentration to ensure complete formation of ligand-bound
528 protein. For the TR-FRET coregulator assay, each well contained 4 nM 6xHis-PPARγ
529 LBD protein (with or without covalent modification by a covalent antagonist), 1 nM
530 LanthaScreen Elite Tb-anti-HIS Antibody (Thermo Fisher Scientific), and 400 nM FITC-
531 labeled TRAP220 or NCoR peptide described above in TR-FRET buffer. Ligand stocks
532 were prepared via serial dilution in DMSO, added to wells in triplicate, and plates were
533 incubated at 25 °C for 1 h and read using BioTek Synergy Neo multimode plate reader.
534 The Tb donor was excited at 340 nm; its fluorescence emission was monitored at 495
535 nm, and the acceptor FITC emission was measured at 520 nm; and the TR-FRET ratio
536 was calculated as the signal at 520 nm divided by the signal at 495 nm. Data were
537 plotted using GraphPad Prism as TR-FRET ratio vs. ligand concentration; TR-FRET
538 coregulator data were fit to sigmoidal dose response curve equation, and ligand
539 displacement data were fit to the one site – Fit K_i binding equation to obtain K_i values
540 using the known binding affinity of Fluormone Pan-PPAR Green (2.8 nM; Invitrogen
541 PV4894 product insert).

542 *Fluorescence polarization coregulator interaction assays*

543 Wild-type or mutant 6xHis-PPARγ LBD in assay buffer (20 mM potassium
544 phosphate (pH 8), 50 mM potassium chloride, 5 mM TCEP, 0.5 mM EDTA, and 0.01%
545 Tween-20) was diluted by serial dilution and plated with 200 nM FITC-labeled
546 TRAP220 or NCoR peptides described above in black 384-well plates (Greiner). The
547 plate was incubated at 4 °C for 1 hr, and fluorescence polarization was measured on a
548 BioTek Synergy Neo multimode plate reader at 485 nm emission and 528 nm excitation
549 wavelengths. Data were plotted using GraphPad Prism as fluorescence polarization
550 signal in millipolarization units vs. protein concentration and fit to a one site total
551 binding equation.

552 *Luciferase reporter assay and western analysis of protein levels*

553 For the luciferase reporter assay, HEK293T cells (ATCC; cat# CRL-3216) were
554 cultured in DMEM media (Gibco) supplemented with 10% fetal bovine serum (FBS) and
555 50 units mL^{-1} of penicillin, streptomycin, and glutamine and grown to 90% confluency
556 in a T-75 flask before seeding 4 million cells per well in 10 cm dishes. Seeded cells were
557 transfected with 4.5 μg of pCMV6-XL4 plasmid containing full-length human PPARγ2
558 and 4.5 μg of 5X-multimerized PPAR response element (PPRE)-luciferase reporter
559 plasmid with 27 μL of X-treme Gene 9 transfection reagent (Roche) in serum-free Opti-
560 mem reduced serum media (Gibco). Following 18 hr incubation at 37 °C in a 5%
561 CO_2 incubator, transfected cells were plated in white 384-well plates (Perkin Elmer) at a
562 density of 10,000 cells per well (20 μL volume). After plating, cells were incubated 4 hr
563 before treatment in quadruplicate with 20 μL of either vehicle control (2% DMSO in
564 DMEM media) or 1:3 serial dilution of ligand (edaglitazone or rosiglitazone) from 2
565 pM– 630 nM; DMSO concentration was constant at 2% in all wells. Following a second
566 18 hr incubation, treated cells were developed with 20 μL Britelite Plus (Perkin Elmer),
567 and luminescence was measured using a BioTek Synergy Neo multimode plate reader.
568 Data were plotted in GraphPad Prism as luminescence vs. ligand concentration and fit
569 to a sigmoidal dose response curve.

570 For the western analysis, HEK293T cells (ATCC; cat# CRL-3216) were transfected
571 described above except in 6-well plates (Corning) with 250,000 cells and 1 μg of
572 pCMV6-XL4 plasmid containing wild-type or mutant full-length human PPARγ2 with 3
573 μL of X-treme Gene 9 and incubated for 48 hr. Transfected cells were then lysed in TNT
574 buffer (150 mM NaCl, 0.1 M Tris, 1% Triton-X 100, pH 7.5) and incubated for 1 hr at
575 4 ˚C. Protein concentration was determined by BCA assay (ThermoFisher). Twenty μg
576 of protein was loaded onto 4-15% gradient gels (Bio-Rad) and wet transferred onto
577 PVDF. The membrane was blocked for 1 hr at room temperature with 5% milk in PBS
578 all antibodies were diluted in 1% milk in PBS. After blocking, the membrane was
579 incubated overnight at 4 ˚C with 1:1000 dilution of rabbit anti-PPARγ (Cell Signaling
580 Technology, #2435). The following day, the blot was washed with PBST and treated
581 with 1:3000 dilution of anti-rabbit IgG-HRP (Cell Signaling Technology, #7074) for 45
582 min at room temperature, then washed with PBST and developed with ECL
583 (ThermoFisher). The membrane was stripped, blocked and re-probed with 1:1000
584 mouse anti-actin (EMD/MilliporeSigma, MAB1501) overnight at 4 ˚C. The following day
585 the blot was washed with PBST and treated with 1:10,000 dilution of anti-mouse IgG-
586 HRP (Sigma Aldrich, #A9917) for 45 min at room temperature, then washed with PBST
587 and developed with ECL (Thermo Fisher).

588 *Crystallization, structure determination, and structural analyses*

589 PPARγ LBD protein was purified as described above. For edaglitazone- and
590 GW9662-PPARγ LBD complexes, protein was incubated at a 1:3 protein/ligand molar
591 ratio in PBS overnight, concentrated to 10 mg/mL, and buffer exchanged. Crystals were
592 obtained after 3–5 days at 22 °C by sitting-drop vapor diffusion against 50 μL of well
593 solution using 96-well format crystallization plates. The crystallization drops contained
594 1 μL of protein/ligand sample mixed with 1 μL of reservoir solution containing 0.1 M
595 Tris-HCl (pH 7.6) and 0.8 M sodium citrate. Crystals for the SR16832-PPARγ LBD
596 complex were obtained via "dry" co-crystallization method (52) after ~14 days using a
597 reservoir solution containing 0.1 M MOPS (pH 7.6) and 0.8 M sodium citrate. All
598 crystals were flash-frozen in liquid nitrogen before data collection. Data collection for
599 the edaglitazone-bound structure was carried out at LS-CAT Beamline 21-ID-D at the
600 Advanced Photon Source at Argonne National Laboratory; the GW9662-bound
601 structure at Beamline 5.0.2 at Berkeley Center for Structural Biology; and the SR16832-
602 bound structure using our home source MicroMax007 HF x-ray generator equipped
603 with the mar345 detector. Data were processed, integrated, and scaled with the
604 programs Mosflm (53) and Scala in CCP4 (54). The structure was solved by molecular
605 replacement using the program Phaser (55) that is implemented in the PHENIX package
606 (56) using a previously published PPARγ LBD structure (PDB code 1PRG) (9) as the
607 search model. The structure was refined using PHENIX with several cycles of
608 interactive model rebuilding in Coot (57). Figures were prepared using PyMOL
609 (Schrödinger), and the orthsoteric pocket and alternate site volumes shown in Figure 1
610 were calculated using HOLLOW (58).

611 *Nonanoic acid fitting into published ligand-bound PPARγ crystal structures*

612 We analyzed several high-resolution crystal structures, including structures
613 where based on sequence information it was possible that Ω-loop density was present,
614 to determine if density consistent with a medium-chain fatty acid could be present. Our
615 analysis included PDB codes 1fm6, 1fm9, 1k74, 1zgy, 2hfp, 2prg, 2q5s, 2q61, 2q6s, 2q6r,
616 2zk1, 2zk2, 2zk3, 2zk4, 2zk5, 2zk6, 2zvt, 3adw, 3b0q, 3qt0, 3r8i, 3t03, 4ema, 4fgy, 4xld,
617 5two. In some cases it was assumed that the potential fatty acid electron density may
618 have been fitted by water molecules in the previous structure determinations near the
619 site where we observed a medium-chain fatty acid in our edaglitazone-bound structure.
620 In other cases, we analyzed the electron density present in mtz files downloaded from
621 the PDBe (e.g., http://www.ebi.ac.uk/pdbe/coordinates/files/xxxx_map.mtz; where xxxx
622 is the PDB code in lower case letters) for unmodeled density. After removal of all water
623 molecules from the PDB structure file, a ligand search followed by interactive real space
624 refinement was performed using the crystallography atomic modeling program Coot
625 (57); this structure was subjected to refinement with rebuilt water molecules using
626 Phenix (56). Of the structures analyzed, nonanoic acid was successfully fitted into the

electron density of PPARγ LBD bound to the TZD ligands rosiglitazone (PDB code 1FM6) and MCC-555 (PDB code 3B0Q), as well as the non-TZD ligands SR145 (PDB code 2Q61) and GQ-16 (PDB code 3T03).

NMR spectroscopy

Two-dimensional (2D) [^{1}H,^{15}N]-transverse relaxation optimized spectroscopy (TROSY)-heteronuclear single quantum correlation (HSQC) data were collected at 298K using a Bruker 700 Mhz NMR instrument equipped with a QCI cryoprobe. Samples contained approximately 200 μM protein in a NMR buffer containing 50 mM potassium phosphate (pH 7.4), 20 mM potassium chloride, 1 mM TCEP, and 10% D_2O. Data were processed and analyzed using Topspin 3.0 (Bruker) and NMRViewJ (OneMoon Scientific, Inc.) (59). NMR analysis was performed using previously described rosiglitazone-bound NMR chemical shift assignments (BMRB entry 17975) (36); for the analysis of PPARγ bound to edaglitazone and/or nonanoic acid, the analysis was limited to well resolved peaks for residues with chemical shift values similar to PPARγ bound to rosiglitazone via the minimum chemical shift procedure (60).

Molecular dynamics simulations

Edaglitazone was modeled with the NH in the thiazolidinedione group (pKa ~6.4 (61)) as deprotonated, thus with a total charge of -1 at physiologic pH. Nonanoic acid (pKa of the carboxyl group is ~5) was modeled as deprotonated and having an overall -1 charge. Appropriate protons were added to edaglitazone and nonanoic acid structures extracted from the crystal structure using Chimera (62) and submitted to REDD server (63). The resulting mol2 files were used in tleap (AMBER version 16) along with the crystal structure bound to edaglitazone and nonanoic acid (PDB code 5UGM). Missing amino acids were added via Modeller (64) within Chimera, including an N-terminal glycine that was added in order to match the NMR construct (vestige of tag cleavage). The structures (without ligand) were run through the H++ server (65) to calculate probable protonation states of titratable protons based on structure. Ligands were then added to the H++ PDB file via overlay of the crystal structure in Chimera. Pdb4amber was used to generate a PDB file with amber names and antechamber was used to give gaff2 names to the ligand mol2 files. Parmchk2 was used to generate force modification files for the ligands with gaff2 parameters. Sodium ions were used to neutralize the ligand-protein complex, and KCl was added to 50 mM (to match the NMR experimental conditions) using TIP3P specific parameters (66). The system was solvated with TIP3P (67) water in a truncated octahedron box at least 10 Angstroms from any protein or ligand atom. FF14SB (68)was used for protein parameters. This build was then minimized and equilibrated in 9 steps with restraints on heavy atoms decreasing with each step with the last minimization and equilibration steps without restraints.

Production runs were then carried out with hydrogen mass repartitioned (69) parameter files to enable 4 fs time steps. Constant pressure replicate production runs were carried out with independent randomized starting velocities. Pressure was controlled with a Monte Carlo barostat and a pressure relaxation time (taup) of 2ps. Temperature was kept constant at 310 K with Langevin dynamics utilizing a collision frequency (gamma_ln) of 3 ps^{-1}. The particle mesh ewald method was used to calculate non-bonded atom interactions with a cutoff (cut) of 8.0 Å. SHAKE (70) was used to allow longer time steps in addition to hydrogen mass repartitioning. Analysis of trajectories was performed using cpptraj (71) and pytraj. Hydrogen bond analysis was performed using dist = 3.5 Å and angle = 100° (72).

Density functional theory calculations

All calculations were performed at B3LYP/6-311 + G (73, 74) level using Gaussian 98 package. In order to reduce the calculation time/computational cost, we used a simplified model by only considering the nonanoic acid-interacting parts of GW9662 (phenyl group), SR16832 (6-methoxyquinoline group) in the calculations. Geometry optimizations were performed for GW9662, SR16832, nonanoic acid, GW9662+nonanoic acid, and SR16832+nonanoic acid using the structural conformations present in the crystal structures.

Authorship Contributions

J.S. and D.J.K. conceived and designed the research. J.S. expressed and purified protein; solved the crystal structures; performed and analyzed NMR and biochemical assays; and analyzed previously solved ligand-bound crystal structures. R.B. and S.A.M. performed cell-based assays. R.B. performed western analysis. J.B. performed site-directed mutagenesis and expressed/purified protein. P.M.-T. performed biochemical assays. T.S.H. built and performed minimization/equilibration of molecular simulation input files; and provided advice on simulations runs and analyses. M.T. and Q.G. performed density functional theory calculations. D.J.K. performed and analyzed molecular simulations, analyzed data, supervised the research, and wrote the manuscript with help from J.S. and input from all authors.

Competing financial interests

The authors declare no competing financial interests.

Acknowledgements

696 This work was supported in part by National Institutes of Health (NIH) grants
697 R01DK101871 (DJK), R00DK103116 (TH), and F32DK108442 (RB); American Heart
698 Association (AHA) fellowship award 16POST27780018 (RB); National Science
699 Foundation (NSF) funding to the Summer Undergraduate Research Fellows (SURF)
700 program at The Scripps Research Institute [Grant 1659594]; and the Academic Year
701 Research Internship for Undergraduates (AYRIU) program at The Scripps Research
702 Institute.

References

1. Soccio RE, Chen ER, Lazar MA. Thiazolidinediones and the promise of insulin sensitization in type 2 diabetes. Cell Metab. 2014;20(4):573-91.

2. Fujita T, Sugiyama Y, Taketomi S, Sohda T, Kawamatsu Y, Iwatsuka H, Suzuoki Z. Reduction of insulin resistance in obese and/or diabetic animals by 5-[4-(1-methylcyclohexylmethoxy)benzyl]-thiazolidine-2,4-dione (ADD-3878, U-63,287, ciglitazone), a new antidiabetic agent. Diabetes. 1983;32(9):804-10.

3. Lehmann JM, Moore LB, Smith-Oliver TA, Wilkison WO, Willson TM, Kliewer SA. An antidiabetic thiazolidinedione is a high affinity ligand for peroxisome proliferator-activated receptor gamma (PPAR gamma). The Journal of biological chemistry. 1995;270(22):12953-6.

4. Gallastegui N, Mackinnon JA, Fletterick RJ, Estebanez-Perpina E. Advances in our structural understanding of orphan nuclear receptors. Trends Biochem Sci. 2015;40(1):25-35.

5. Kroker AJ, Bruning JB. Review of the structural and dynamic mechanisms of PPARγ partial agonism. PPAR Res. 2015;816856:1-15.

6. Edman K, Hosseini A, Bjursell MK, Aagaard A, Wissler L, Gunnarsson A, Kaminski T, Kohler C, Backstrom S, Jensen TJ, Cavallin A, Karlsson U, Nilsson E, Lecina D, Takahashi R, Grebner C, Geschwindner S, Lepisto M, Hogner AC, Guallar V. Ligand Binding Mechanism in Steroid Receptors: From Conserved Plasticity to Differential Evolutionary Constraints. Structure. 2015;23(12):2280-90.

7. Aci-Seche S, Genest M, Garnier N. Ligand entry pathways in the ligand binding domain of PPARgamma receptor. FEBS letters. 2011;585(16):2599-603.

8. Genest D, Garnier N, Arrault A, Marot C, Morin-Allory L, Genest M. Ligand-escape pathways from the ligand-binding domain of PPARgamma receptor as probed by molecular dynamics simulations. Eur Biophys J. 2008;37(4):369-79.

9. Nolte RT, Wisely GB, Westin S, Cobb JE, Lambert MH, Kurokawa R, Rosenfeld MG, Willson TM, Glass CK, Milburn MV. Ligand binding and co-activator assembly of the peroxisome proliferator-activated receptor-gamma. Nature. 1998;395(6698):137-43.

10. Itoh T, Fairall L, Amin K, Inaba Y, Szanto A, Balint BL, Nagy L, Yamamoto K, Schwabe JW. Structural basis for the activation of PPARgamma by oxidized fatty acids. Nat Struct Mol Biol. 2008.

11. Li Y, Zhang J, Schopfer FJ, Martynowski D, Garcia-Barrio MT, Kovach A, Suino-Powell K, Baker PR, Freeman BA, Chen YE, Xu HE. Molecular recognition of nitrated fatty acids by PPAR gamma. Nat Struct Mol Biol. 2008;15(8):865-7.

12. Malapaka RR, Khoo S, Zhang J, Choi JH, Zhou XE, Xu Y, Gong Y, Li J, Yong EL, Chalmers MJ, Chang L, Resau JH, Griffin PR, Chen YE, Xu HE. Identification and mechanism of 10-carbon fatty acid as modulating ligand of peroxisome proliferator-activated receptors. The Journal of biological chemistry. 2012;287(1):183-95.

13. Waku T, Shiraki T, Oyama T, Fujimoto Y, Maebara K, Kamiya N, Jingami H, Morikawa K. Structural insight into PPARgamma activation through covalent modification with endogenous fatty acids. J Mol Biol. 2009;385(1):188-99.

14. Waku T, Shiraki T, Oyama T, Morikawa K. Atomic structure of mutant PPARgamma LBD complexed with 15d-PGJ2: novel modulation mechanism of PPARgamma/RXRalpha function by covalently bound ligands. FEBS letters. 2009;583(2):320-4.

15. Kliewer SA, Sundseth SS, Jones SA, Brown PJ, Wisely GB, Koble CS, Devchand P, Wahli W, Willson TM, Lenhard JM, Lehmann JM. Fatty acids and eicosanoids regulate gene expression through direct interactions with peroxisome proliferator-activated receptors alpha and gamma. Proc Natl Acad Sci U S A. 1997;94(9):4318-23.

16. Ziouzenkova O, Perrey S, Asatryan L, Hwang J, MacNaul KL, Moller DE, Rader DJ, Sevanian A, Zechner R, Hoefler G, Plutzky J. Lipolysis of triglyceride-rich lipoproteins generates PPAR ligands: evidence for an antiinflammatory role for lipoprotein lipase. Proc Natl Acad Sci U S A. 2003;100(5):2730-5.

17. Xu HE, Lambert MH, Montana VG, Parks DJ, Blanchard SG, Brown PJ, Sternbach DD, Lehmann JM, Wisely GB, Willson TM, Kliewer SA, Milburn MV. Molecular recognition of fatty acids by peroxisome proliferator-activated receptors. Mol Cell. 1999;3(3):397-403.

18. Nagy L, Tontonoz P, Alvarez JG, Chen H, Evans RM. Oxidized LDL regulates macrophage gene expression through ligand activation of PPARgamma. Cell. 1998;93(2):229-40.

19. Hughes TS, Shang J, Brust R, de Vera IM, Fuhrmann J, Ruiz C, Cameron MD, Kamenecka TM, Kojetin DJ. Probing the Complex Binding Modes of the PPARgamma Partial Agonist 2-Chloro-N-(3-chloro-4-((5-chlorobenzo[d]thiazol-2-yl)thio)phenyl)-4-(trifluorome

thyl)benzenesulfonamide (T2384) to Orthosteric and Allosteric Sites with NMR Spectroscopy. J Med Chem. 2016;59(22):10335-41.

20. Li Y, Wang Z, Furukawa N, Escaron P, Weiszmann J, Lee G, Lindstrom M, Liu J, Liu X, Xu H, Plotnikova O, Prasad V, Walker N, Learned RM, Chen JL. T2384, a novel antidiabetic agent with unique peroxisome proliferator-activated receptor gamma binding properties. The Journal of biological chemistry. 2008;283(14):9168-76.

21. Hughes TS, Giri PK, de Vera IM, Marciano DP, Kuruvilla DS, Shin Y, Blayo AL, Kamenecka TM, Burris TP, Griffin PR, Kojetin DJ. An alternate binding site for PPARγ ligands. Nature communications. 2014;5:3571.

22. Brust R, Lin H, Fuhrmann J, Asteian A, Kamenecka TM, Kojetin DJ. Modification of the Orthosteric PPARgamma Covalent Antagonist Scaffold Yields an Improved Dual-Site Allosteric Inhibitor. ACS Chem Biol. 2017;12(4):969-78.

23. Jang JY, Koh M, Bae H, An DR, Im HN, Kim HS, Yoon JY, Yoon HJ, Han BW, Park SB, Suh SW. Structural basis for differential activities of enantiomeric PPARgamma agonists: Binding of S35 to the alternate site. Biochim Biophys Acta. 2017;1865(6):674-81.

24. Bae H, Jang JY, Choi CS-S, Lee J-J, Kim H, Jo A, Lee K-J, Choi JC, Suh SW, Park SB. Mechanistic elucidation guided by covalent inhibitors for the development of anti-diabetic PPARγ ligands. Chem Sci. 2016;7:5523-9.

25. Choi JH, Banks AS, Estall JL, Kajimura S, Bostrom P, Laznik D, Ruas JL, Chalmers MJ, Kamenecka TM, Bluher M, Griffin PR, Spiegelman BM. Anti-diabetic drugs inhibit obesity-linked phosphorylation of PPARgamma by Cdk5. Nature. 2010;466(7305):451-6.

26. Choi JH, Banks AS, Kamenecka TM, Busby SA, Chalmers MJ, Kumar N, Kuruvilla DS, Shin Y, He Y, Bruning JB, Marciano DP, Cameron MD, Laznik D, Jurczak MJ, Schurer SC, Vidovic D, Shulman GI, Spiegelman BM, Griffin PR. Antidiabetic actions of a non-agonist PPARgamma ligand blocking Cdk5-mediated phosphorylation. Nature. 2011;477(7365):477-81.

27. Choi SS, Kim ES, Koh M, Lee SJ, Lim D, Yang YR, Jang HJ, Seo KA, Min SH, Lee IH, Park SB, Suh PG, Choi JH. A novel non-agonist peroxisome proliferator-activated receptor gamma (PPARgamma) ligand UHC1 blocks PPARgamma phosphorylation by cyclin-dependent kinase 5 (CDK5) and improves insulin sensitivity. The Journal of biological chemistry. 2014;289(38):26618-29.

28. Dietz M, Mohr P, Kuhn B, Maerki HP, Hartman P, Ruf A, Benz J, Grether U, Wright MB. Comparative molecular profiling of the PPARalpha/gamma activator aleglitazar: PPAR selectivity, activity and interaction with cofactors. ChemMedChem. 2012;7(6):1101-11.

29. Furnsinn C, Brunmair B, Meyer M, Neschen S, Furtmuller R, Roden M, Kuhnle HF, Nowotny P, Schneider B, Waldhausl W. Chronic and acute effects of thiazolidinediones

BM13.1258 and BM15.2054 on rat skeletal muscle glucose metabolism. Br J Pharmacol. 1999;128(6):1141-8.

30. Liberato MV, Nascimento AS, Ayers SD, Lin JZ, Cvoro A, Silveira RL, Martinez L, Souza PC, Saidemberg D, Deng T, Amato AA, Togashi M, Hsueh WA, Phillips K, Palma MS, Neves FA, Skaf MS, Webb P, Polikarpov I. Medium chain fatty acids are selective peroxisome proliferator activated receptor (PPAR) gamma activators and pan-PPAR partial agonists. PloS one. 2012;7(5):e36297.

31. Kabsch W, Sander C. Dictionary of protein secondary structure: pattern recognition of hydrogen-bonded and geometrical features. Biopolymers. 1983;22(12):2577-637.

32. Gampe RT, Jr., Montana VG, Lambert MH, Miller AB, Bledsoe RK, Milburn MV, Kliewer SA, Willson TM, Xu HE. Asymmetry in the PPARgamma/RXRalpha crystal structure reveals the molecular basis of heterodimerization among nuclear receptors. Mol Cell. 2000;5(3):545-55.

33. Bruning JB, Chalmers MJ, Prasad S, Busby SA, Kamenecka TM, He Y, Nettles KW, Griffin PR. Partial agonists activate PPARgamma using a helix 12 independent mechanism. Structure. 2007;15(10):1258-71.

34. Amato AA, Rajagopalan S, Lin JZ, Carvalho BM, Figueira AC, Lu J, Ayers SD, Mottin M, Silveira RL, Souza PC, Mourao RH, Saad MJ, Togashi M, Simeoni LA, Abdalla DS, Skaf MS, Polikparpov I, Lima MC, Galdino SL, Brennan RG, Baxter JD, Pitta IR, Webb P, Phillips KJ, Neves FA. GQ-16, a novel peroxisome proliferator-activated receptor gamma (PPARgamma) ligand, promotes insulin sensitization without weight gain. The Journal of biological chemistry. 2012;287(33):28169-79.

35. Tao H, Bausch C, Richmond C, Blattner FR, Conway T. Functional genomics: expression analysis of Escherichia coli growing on minimal and rich media. J Bacteriol. 1999;181(20):6425-40.

36. Hughes TS, Chalmers MJ, Novick S, Kuruvilla DS, Chang MR, Kamenecka TM, Rance M, Johnson BA, Burris TP, Griffin PR, Kojetin DJ. Ligand and receptor dynamics contribute to the mechanism of graded PPARγ agonism. Structure. 2012;20(1):139-50.

37. Puhl AC, Bernardes A, Silveira RL, Yuan J, Campos JL, Saidemberg DM, Palma MS, Cvoro A, Ayers SD, Webb P, Reinach PS, Skaf MS, Polikarpov I. Mode of Peroxisome Proliferator-Activated Receptor gamma Activation by Luteolin. Molecular pharmacology. 2012;81(6):788-99.

38. Waku T, Shiraki T, Oyama T, Maebara K, Nakamori R, Morikawa K. The nuclear receptor PPARgamma individually responds to serotonin- and fatty acid-metabolites. The EMBO journal. 2010;29(19):3395-407.

39. Leesnitzer LM, Parks DJ, Bledsoe RK, Cobb JE, Collins JL, Consler TG, Davis RG, Hull-Ryde EA, Lenhard JM, Patel L, Plunket KD, Shenk JL, Stimmel JB, Therapontos C, Willson TM, Blanchard SG. Functional consequences of cysteine modification in the ligand binding sites of peroxisome proliferator activated receptors by GW9662. Biochemistry. 2002;41(21):6640-50.

40. Lee G, Elwood F, McNally J, Weiszmann J, Lindstrom M, Amaral K, Nakamura M, Miao S, Cao P, Learned RM, Chen JL, Li Y. T0070907, a selective ligand for peroxisome proliferator-activated receptor gamma, functions as an antagonist of biochemical and cellular activities. The Journal of biological chemistry. 2002;277(22):19649-57.

41. Marciano DP, Kuruvilla DS, Boregowda SV, Asteian A, Hughes TS, Garcia-Ordonez R, Corzo CA, Khan TM, Novick SJ, Park H, Kojetin DJ, Phinney DG, Bruning JB, Kamenecka TM, Griffin PR. Pharmacological repression of PPARgamma promotes osteogenesis. Nature communications. 2015;6:7443.

42. Palusiak M, Grabowski SJ. Methoxy group as an acceptor of proton in hydrogen bonds. J Mol Struct. 2002;642(1-3):97-104.

43. Egea PF, Mitschler A, Moras D. Molecular recognition of agonist ligands by RXRs. Mol Endocrinol. 2002;16(5):987-97.

44. Scheepstra M, Leysen S, van Almen GC, Miller JR, Piesvaux J, Kutilek V, van Eenennaam H, Zhang H, Barr K, Nagpal S, Soisson SM, Kornienko M, Wiley K, Elsen N, Sharma S, Correll CC, Trotter BW, van der Stelt M, Oubrie A, Ottmann C, Parthasarathy G, Brunsveld L. Identification of an allosteric binding site for RORgammat inhibition. Nature communications. 2015;6:8833.

45. Delfosse V, Dendele B, Huet T, Grimaldi M, Boulahtouf A, Gerbal-Chaloin S, Beucher B, Roecklin D, Muller C, Rahmani R, Cavailles V, Daujat-Chavanieu M, Vivat V, Pascussi JM, Balaguer P, Bourguet W. Synergistic activation of human pregnane X receptor by binary cocktails of pharmaceutical and environmental compounds. Nature communications. 2015;6:8089.

46. Schonfeld P, Wojtczak L. Short- and medium-chain fatty acids in energy metabolism: the cellular perspective. J Lipid Res. 2016;57(6):943-54.

47. Nagao K, Yanagita T. Medium-chain fatty acids: functional lipids for the prevention and treatment of the metabolic syndrome. Pharmacol Res. 2010;61(3):208-12.

48. Kim YG, Lou AC, Saghatelian A. A metabolomics strategy for detecting protein-metabolite interactions to identify natural nuclear receptor ligands. Mol Biosyst. 2011;7(4):1046-9.

49. Itoh T, Fairall L, Amin K, Inaba Y, Szanto A, Balint BL, Nagy L, Yamamoto K, Schwabe JW. Structural basis for the activation of PPARgamma by oxidized fatty acids. Nat Struct Mol Biol. 2008;15(9):924-31.

50. Bligh EG, Dyer WJ. A rapid method of total lipid extraction and purification. Can J Biochem Physiol. 1959;37(8):911-7.

51. Armstrong EH, Goswami D, Griffin PR, Noy N, Ortlund EA. Structural basis for ligand regulation of the fatty acid-binding protein 5, peroxisome proliferator-activated receptor beta/delta (FABP5-PPARbeta/delta) signaling pathway. The Journal of biological chemistry. 2014;289(21):14941-54.

52. Gelin M, Delfosse V, Allemand F, Hoh F, Sallaz-Damaz Y, Pirocchi M, Bourguet W, Ferrer JL, Labesse G, Guichou JF. Combining 'dry' co-crystallization and in situ diffraction to facilitate ligand screening by X-ray crystallography. Acta crystallographica Section D, Biological crystallography. 2015;71(Pt 8):1777-87.

53. Battye TG, Kontogiannis L, Johnson O, Powell HR, Leslie AG. iMOSFLM: a new graphical interface for diffraction-image processing with MOSFLM. Acta crystallographica Section D, Biological crystallography. 2011;67(Pt 4):271-81.

54. Winn MD, Ballard CC, Cowtan KD, Dodson EJ, Emsley P, Evans PR, Keegan RM, Krissinel EB, Leslie AG, McCoy A, McNicholas SJ, Murshudov GN, Pannu NS, Potterton EA, Powell HR, Read RJ, Vagin A, Wilson KS. Overview of the CCP4 suite and current developments. Acta crystallographica Section D, Biological crystallography. 2011;67(Pt 4):235-42.

55. McCoy AJ, Grosse-Kunstleve RW, Adams PD, Winn MD, Storoni LC, Read RJ. Phaser crystallographic software. Journal of applied crystallography. 2007;40(Pt 4):658-74.

56. Adams PD, Afonine PV, Bunkoczi G, Chen VB, Davis IW, Echols N, Headd JJ, Hung LW, Kapral GJ, Grosse-Kunstleve RW, McCoy AJ, Moriarty NW, Oeffner R, Read RJ, Richardson DC, Richardson JS, Terwilliger TC, Zwart PH. PHENIX: a comprehensive Python-based system for macromolecular structure solution. Acta crystallographica Section D, Biological crystallography. 2010;66(Pt 2):213-21.

57. Emsley P, Cowtan K. Coot: model-building tools for molecular graphics. Acta crystallographica Section D, Biological crystallography. 2004;60(Pt 12 Pt 1):2126-32.

58. Ho BK, Gruswitz F. HOLLOW: generating accurate representations of channel and interior surfaces in molecular structures. BMC Struct Biol. 2008;8:49.

59. Johnson BA. Using NMRView to visualize and analyze the NMR spectra of macromolecules. Methods Mol Biol. 2004;278:313-52.

60. Williamson MP. Using chemical shift perturbation to characterise ligand binding. Progress in nuclear magnetic resonance spectroscopy. 2013;73:1-16.

61. Giaginis C, Theocharis S, Tsantili-Kakoulidou A. A consideration of PPAR-gamma ligands with respect to lipophilicity: current trends and perspectives. Expert Opin Investig Drugs. 2007;16(4):413-7.

62. Pettersen EF, Goddard TD, Huang CC, Couch GS, Greenblatt DM, Meng EC, Ferrin TE. UCSF Chimera--a visualization system for exploratory research and analysis. Journal of computational chemistry. 2004;25(13):1605-12.

63. Dupradeau FY, Pigache A, Zaffran T, Savineau C, Lelong R, Grivel N, Lelong D, Rosanski W, Cieplak P. The R.E.D. tools: advances in RESP and ESP charge derivation and force field library building. Phys Chem Chem Phys. 2010;12(28):7821-39.

64. Sali A, Blundell TL. Comparative protein modelling by satisfaction of spatial restraints. J Mol Biol. 1993;234(3):779-815.

65. Anandakrishnan R, Aguilar B, Onufriev AV. H++ 3.0: automating pK prediction and the preparation of biomolecular structures for atomistic molecular modeling and simulations. Nucleic Acids Res. 2012;40(Web Server issue):W537-41.

66. Joung IS, Cheatham TE, 3rd. Molecular dynamics simulations of the dynamic and energetic properties of alkali and halide ions using water-model-specific ion parameters. J Phys Chem B. 2009;113(40):13279-90.

67. Jorgensen WL, Chandrasekhar J, Madura JD, Impey RW, Klein ML. Comparison of simple potential functions for simulating liquid water. J Chem Phys. 1983;79(2):926-35.

68. Maier JA, Martinez C, Kasavajhala K, Wickstrom L, Hauser KE, Simmerling C. ff14SB: Improving the Accuracy of Protein Side Chain and Backbone Parameters from ff99SB. J Chem Theory Comput. 2015;11(8):3696-713.

69. Hopkins CW, Le Grand S, Walker RC, Roitberg AE. Long-Time-Step Molecular Dynamics through Hydrogen Mass Repartitioning. J Chem Theory Comput. 2015;11(4):1864-74.

70. Ryckaert JP, Ciccotti G, Berendsen HJC. Numerical integration of the cartesian equations of motion of a system with constraints: molecular dynamics of n-alkanes. J Comput Phys. 1977;23(3):327-41.

71. Roe DR, Cheatham TEI. PTRAJ and CPPTRAJ: Software for Processing and Analysis of Molecular Dynamics Trajectory Data. J Chem Theory Comput. 2013;9(7):3084-95.

72. Fabiola F, Bertram R, Korostelev A, Chapman MS. An improved hydrogen bond potential: impact on medium resolution protein structures. Protein Sci. 2002;11(6):1415-23.

73. Perdew JP, Burke K, Ernzerhof M. Generalized gradient approximation made simple. Phys Rev Lett. 1996;77(18):3865-8.

74. Parr R, Yang W. Density-Functional Theory of Atoms and Molecules Oxford Univ. Press, New York. 1989.

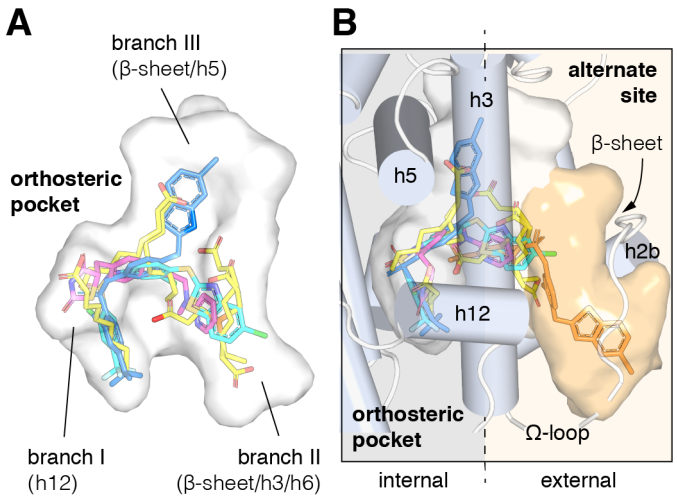

Figure 1. Structural locations of PPARγ orthosteric pocket and alternate site.

(**A**) The T/Y-shaped orthosteric pocket can accommodate one or more natural ligands such as nonanoic acid (yellow sticks; PDB code 4EM9) and synthetic ligands such as rosiglitazone (pink sticks; PDB code 4EMA) or T2384 (light and dark blue sticks representing different crystallized binding modes; PDB code 3K8S, chain A and B, respectively). (**B**) The orthosteric pocket (white pocket surface) is completely enclosed within the alpha helical sandwich fold of the ligand-binding domain (LBD). Ligands such as T2384 (orange sticks; PDB code 3K8S, chain B) can also bind to a solvent accessible alternate site (orange pocket surface) distinct from the orthosteric pocket, structurally defined as the region between helix 3 (h3) and the flexible Ω-loop (dotted line separating the region internal to the LBD, grey background; and external to the LBD, light orange background).

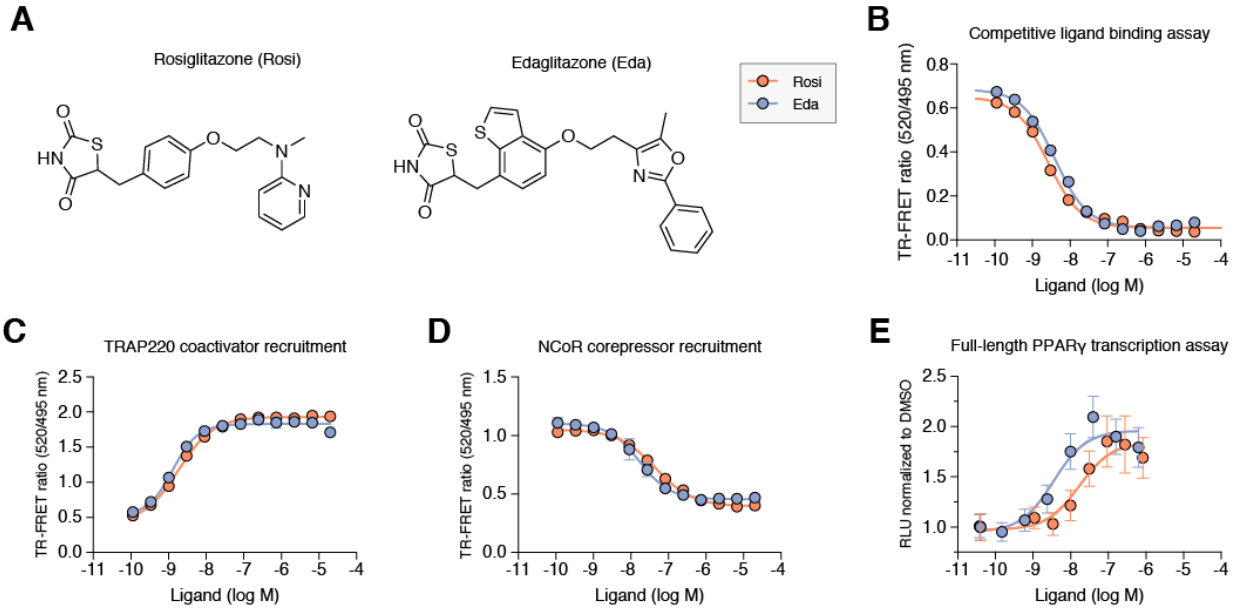

Figure 2. Edaglitazone is a thiazolidinedione (TZD) PPARγ agonist related to rosiglitazone.

(**A**) Chemical structures of edaglitazone and rosiglitazone. (**B**) TR-FRET ligand displacement assay. Data plotted as the average and S.D. of three experimental replicates. (**C,D**) TR-FRET coregulator interaction assay data in the presence of peptides derived from (**C**) TRAP220 coactivator and (**D**) NCoR corepressor. Data plotted as the average and S.D. of three experimental replicates. (**E**) Cell-based luciferase reporter assay measuring full-length PPARγ transcription in HEK293T cells; RLU = relative luciferase units. Data plotted as the average and S.E.M. of four experimental replicates.

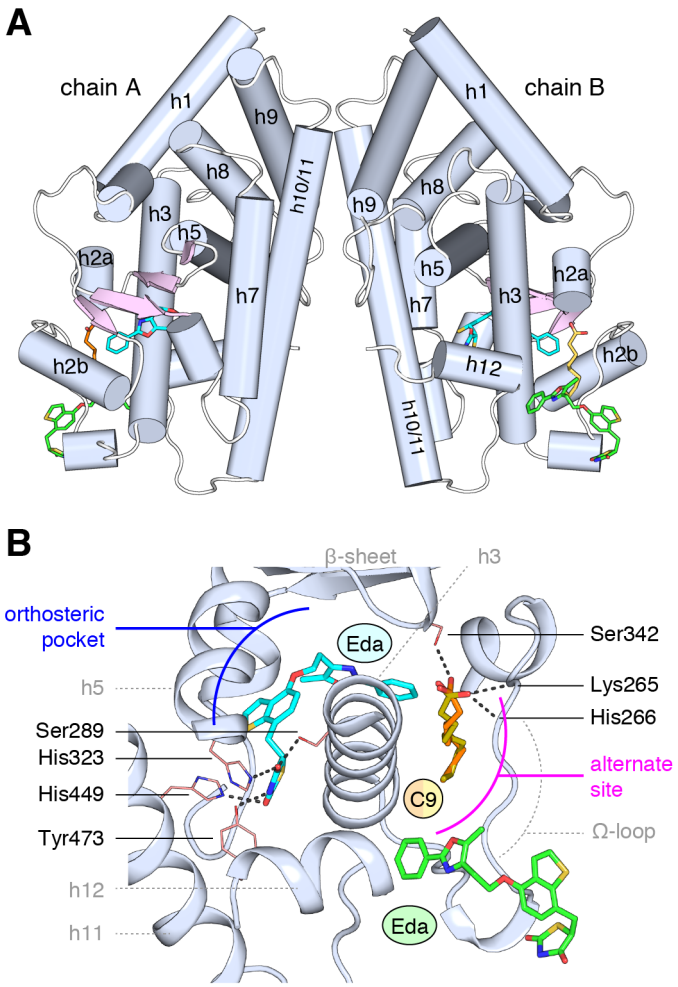

Figure 3. Crystal structure of PPARγ bound to edaglitazone and nonanoic acid.

(**A**) Overall structure (helices, light blue; strands, pink) with two bound edaglitazone (EDA) ligands, one to the canonical orthosteric pocket (blue) and another to a surface pocket (green), and a nonanoic acid (C9) ligand bound to an alternate site (yellow and orange in chain A and B, respectively). (**B**) Molecular interactions between PPARγ and the EDA and C9 ligands. Dotted lines denote hydrogen bonds.

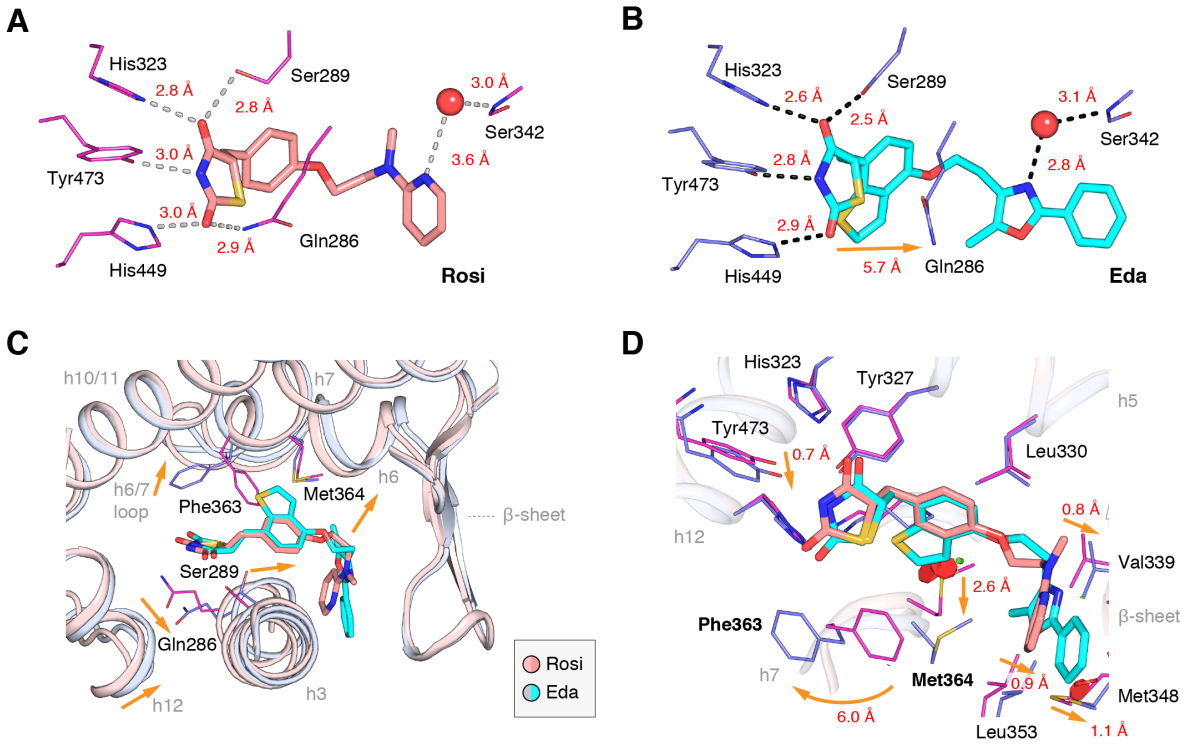

Figure 4. Structural rearrangements that accommodate edaglitazone vs. rosiglitazone binding.

(**A,B**) Comparison of the hydrogen bond interactions between PPARγ and (**A**) rosiglitazone (PDB code 2PRG) and (**B**) edaglitazone. Dotted lines denote hydrogen bonds. (**C,D**) Conformational changes relative to rosiglitazone-bound PPARγ (PDB code 2PRG) that allow the orthosteric pocket to adapt to binding the bulkier benzo[*b*]thiophene moiety in edaglitazone. The changes (orange arrows) include (**C**) shifting of the backbone of helix 3, helix 6, helix 6/7 loop, and helix 12; and (**D**) large movements of the Phe363 and Met364 side chains adjacent to the benzo[*b*]thiophene moiety.

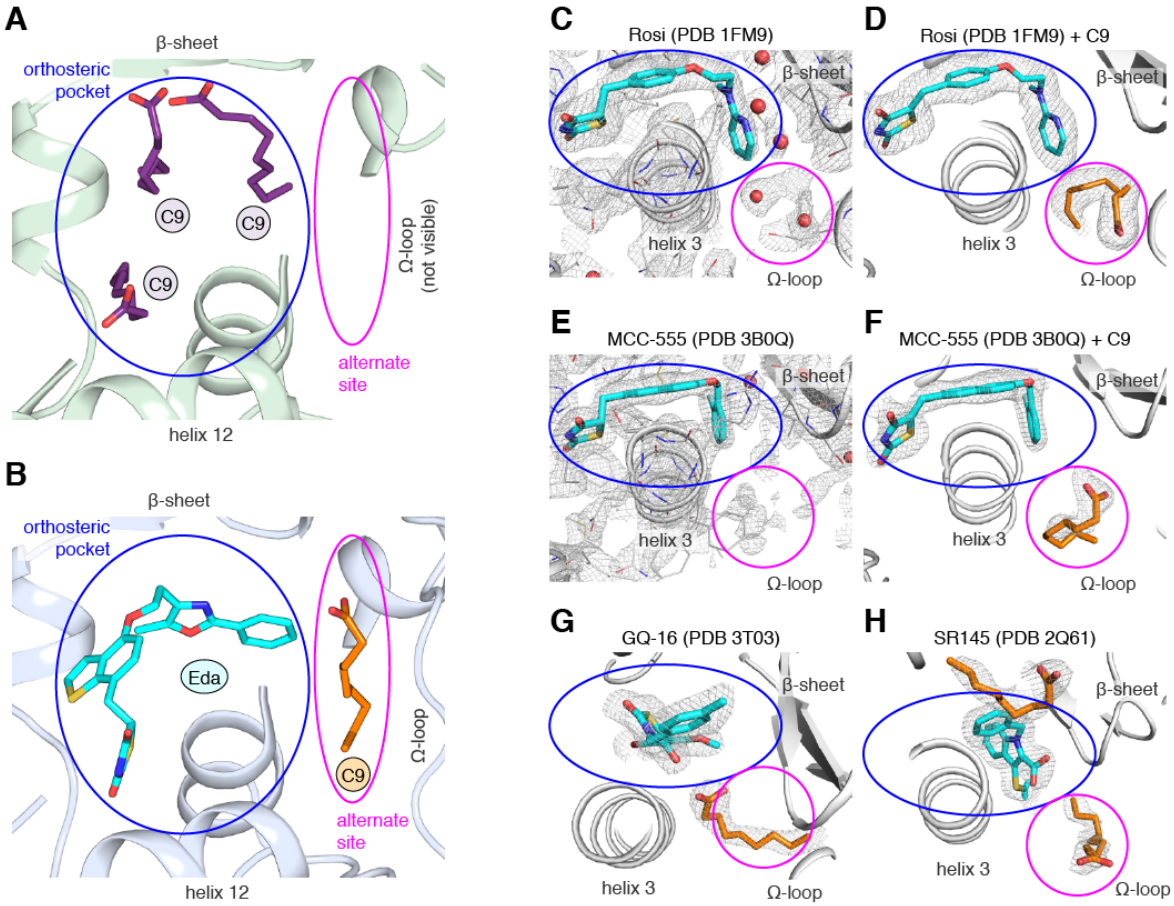

Figure 5. Medium-chain fatty acid density in previously solved synthetic ligand-bound PPARγ crystal structures.

(**A,B**) Comparison of a crystal structure of PPARγ LBD with (**A**) three molecule of nonanoic acid (C9) bound to the orthosteric pocket (PDB code 4EM9) and (**B**) nonanoic acid bound to the alternate site with edaglitazone bound to the orthosteric pocket (PDB code 5UGM). (**C-F**) Electron density maps for previously determined TZD-bound (blue) crystal structures shown with (**C,E**) original deposited structural models and (**D,F**) nonanoic acid (orange) modeled and refined into density present in the alternate site. (G,H) Nonanoic acid (orange) modeled and refined into previously determined crystal structures of PPARγ bound to (**G**) GQ-16 (blue) and (**H**) SR145 (blue). Omit maps ($2F_o–F_c$) contoured at 1 σ in all but the nonanoic acid modeled into the GQ-16 structure, which was contoured at 0.5 σ. The orthosteric pocket and alternate site are circled in blue and magenta, respectively.

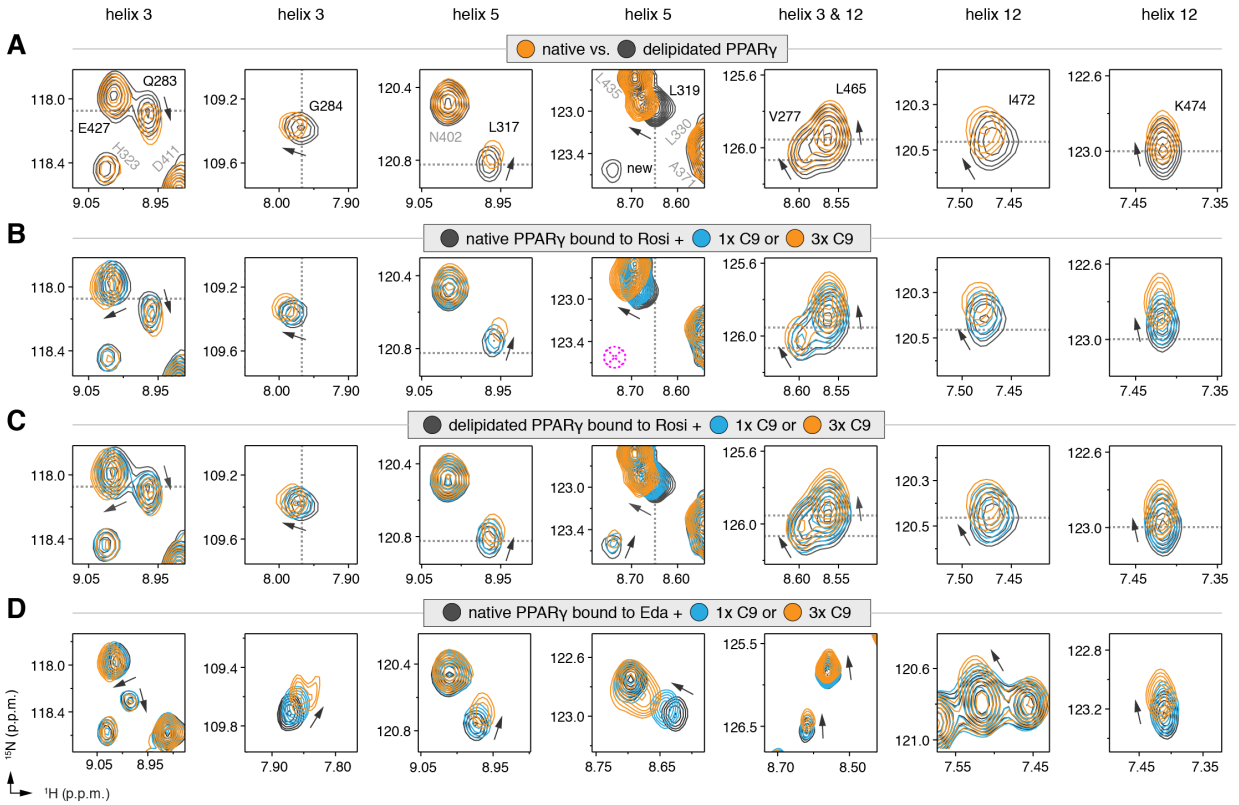

Figure 6. NMR confirms cobinding of nonanoic acid and TZDs.

Differential 2D [^{1}H,^{15}N]-TROSY-HSQC NMR data comparing (**A**) native vs. delipidated PPARγ bound to rosiglitazone (2 equiv.); (**B**) C9 added into native PPARγ bound to rosiglitazone (2 equiv.); (**C**) C9 added into delipidated PPARγ bound to rosiglitazone (2 equiv.); and (**D**) C9 added into native PPARγ bound to edaglitazone (2 equiv.). The dotted lines in panels A–C represent the vertical (^{1}H chemical shift) or horizontal (^{15}N chemical shift) position of the peaks in the delipidated form to illustrate how the peaks corresponding to the native, nondelpidated form shift "on path" to changes caused by C9 binding. Black arrows denote the chemical shift changes; pink dotted circle/cross denotes a missing peak; and dotted lines denote the delipidated apo-PPARγ peak positions to illustrate the "on path" transitions of native and C9-

bound forms.

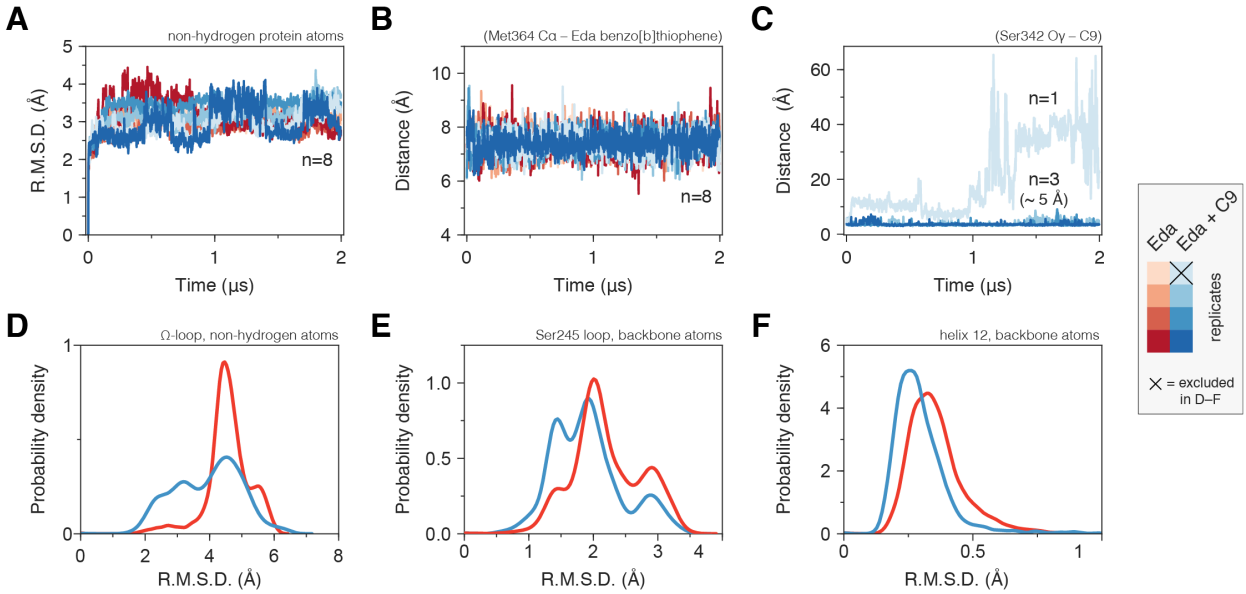

Figure 7. Molecular simulations reveal ligand cobinding stabilizes functionally important regions.

(**A**) Heavy atom R.M.S.D. to the starting conformation (crystal structure after minimization and equilibration) reveal that all four simulations bound to edaglitazone only to the orthosteric site (red lines) or cobound to nonanoic acid at the alternate site (blue lines) are stable during the simulation period. (**B**) Distance between benzo[b]thiophene group in edaglitazone and the Met364 Cα atom shows that edaglitazone remains stably bound to the orthosteric pocket in all eight simulations. (**C**) Nonanoic acid remains stably bound to the alternate site in three of four cobound simulations. In the legend, × denotes the Eda + C9 (light blue) simulation where C9 unbound during the simulation, which was excluded from the analysis. (**D–F**) Probability density histogram distributions of the R.M.S.D. relative to the starting structure for (**D**) the Ω-

loop, (**E**) the loop containing the serine residue phosphorylated by Cdk5, and (**F**) helix 12.

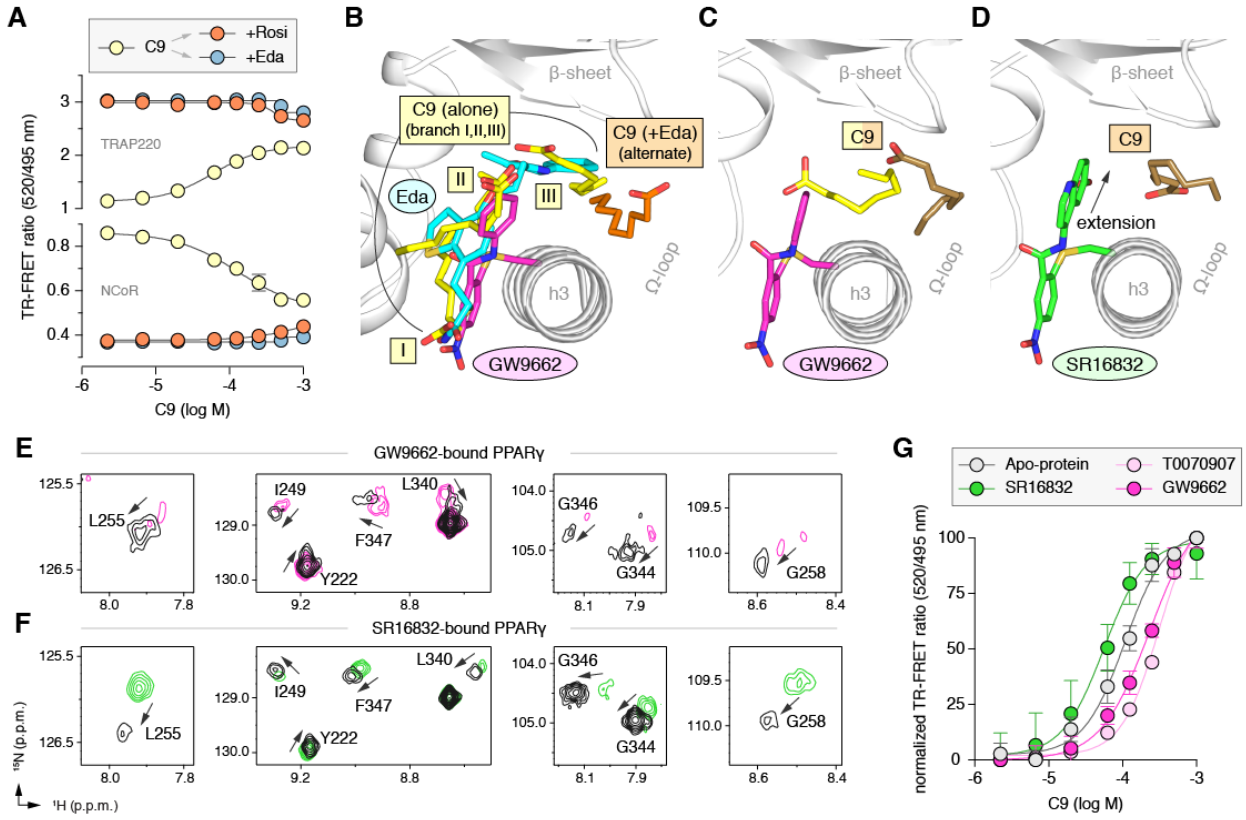

Figure 8. Covalent antagonists illuminate the structural and functional consequences of nonanoic acid cobinding.

(**A**) TR-FRET assays performed in the absence and presence of a saturating concentration (1 μM) of rosiglitazone or edaglitazone. Data plotted as the average and S.D. of three experimental replicates. (**B**) The covalent antagonist GW9662 (PDB code 3B0R; magenta ligand) overlaps with the crystallized binding modes of 2 of 3 nonanoic acid molecules bound to the orthosteric pocket (PDB code 4em9) but not nonanoic acid bound to the alternate site (PDB code 5UGM). (**C,D**) Crystal structures of PPARγ bound to covalent antagonists (**C**) GW9662 and (**D**) SR16832 cobound to nonanoic acid. (**E,F**) Differential 2D [^{1}H,^{15}N]-TROSY-HSQC NMR data of PPARγ covalently bound to (**E**) GW9662 (magenta peaks) and (**F**) SR16832 (green peaks) confirming cobinding to nonanoic acid (black peaks; 2 equiv.). Black arrows denote the chemical shift changes. (**G**) TRAP220-based TR-FRET assay performed in the absence or presence of covalent

antagonists. Data plotted as the average and S.D. of three experimental replicates.

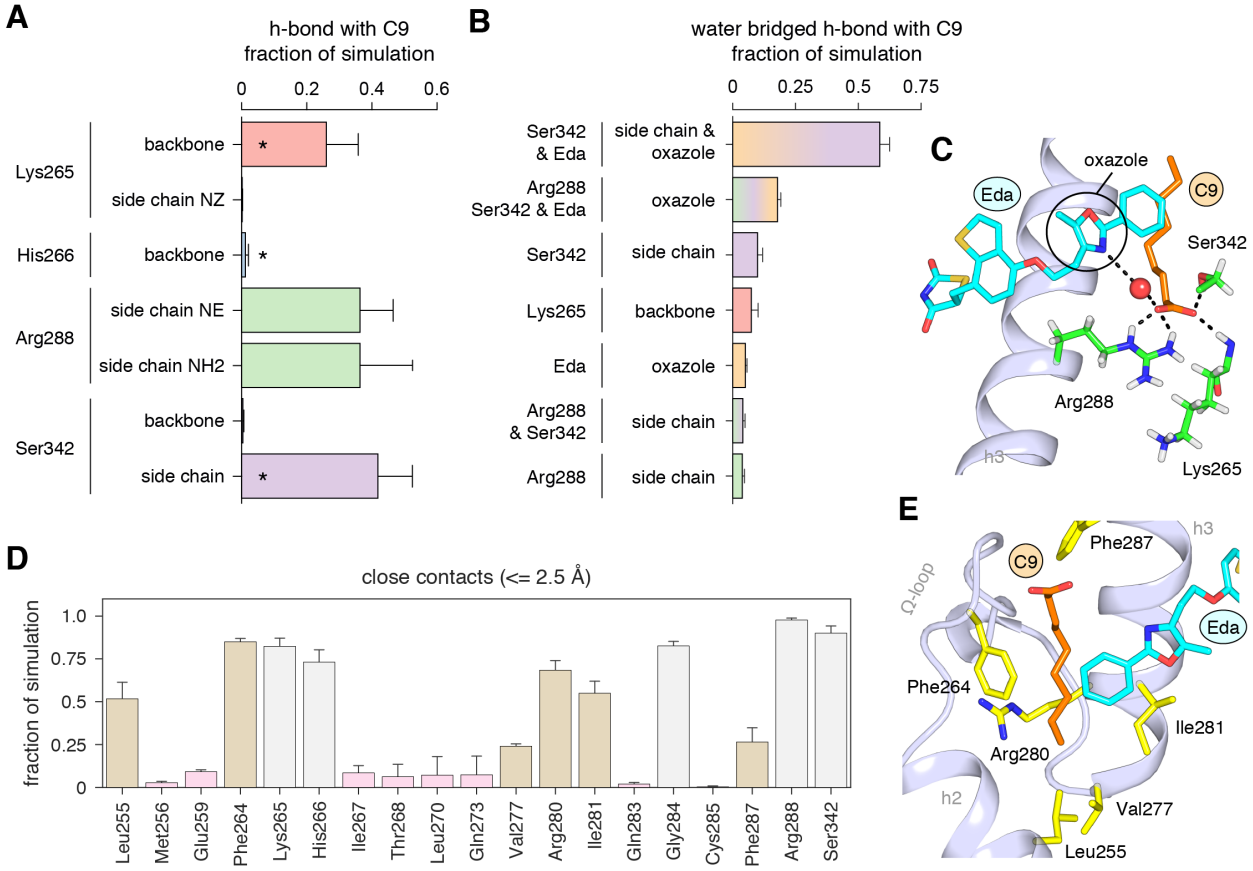

Figure 9. Interactions driving cobinding of nonanoic acid to the alternate site.

(**A**) Direct and (**B**) water-bridged hydrogen bonds detected in the three 2 μs molecular simulations where nonanoic acid remained stably bound; * denotes hydrogen bonds observed in crystal structure. Data plotted as the average and S.D. of three experimental replicates. (**C**) Example of the nonanoic acid-mediated hydrogen bond network from a snapshot of the simulation trajectory. (**D**) Close atomic contacts populated in the simulation (brown, hydrophobic side chain contacts; grey, other contacts; pink, lower abundance contacts). Data plotted as the average and S.D. of three experimental replicates. (**E**) Structural example of the hydrophobic contacts (brown bars in **D**).

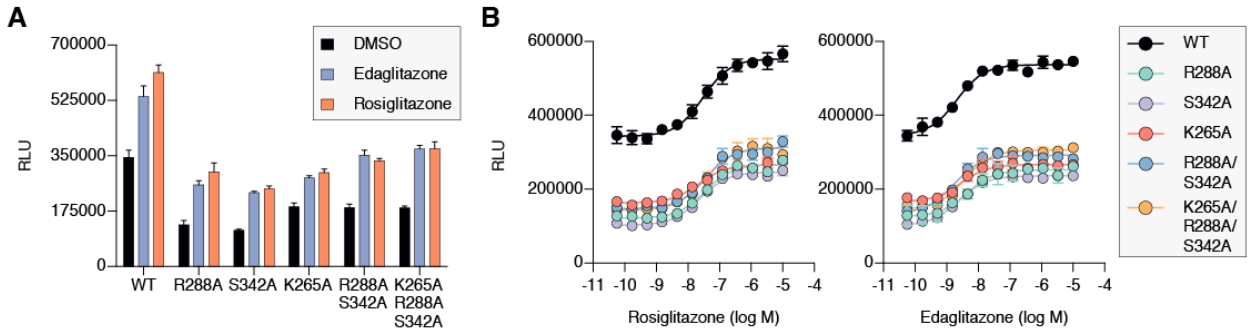

Figure 10. Mutation of residues that form hydrogen bonds with nonanoic acid decrease cellular PPARγ activation and synthetic ligand synergy.

Cell-based luciferase reporter assay measuring full-length wild-type and mutant PPARγ transcription in HEK293T cells treated with ligand in (**A**) single-point (10 μM) and (**B**) dose-response format. Data plotted as the average and S.D. of four experimental replicates; dose response data were fit to a sigmoidal dose response equation.

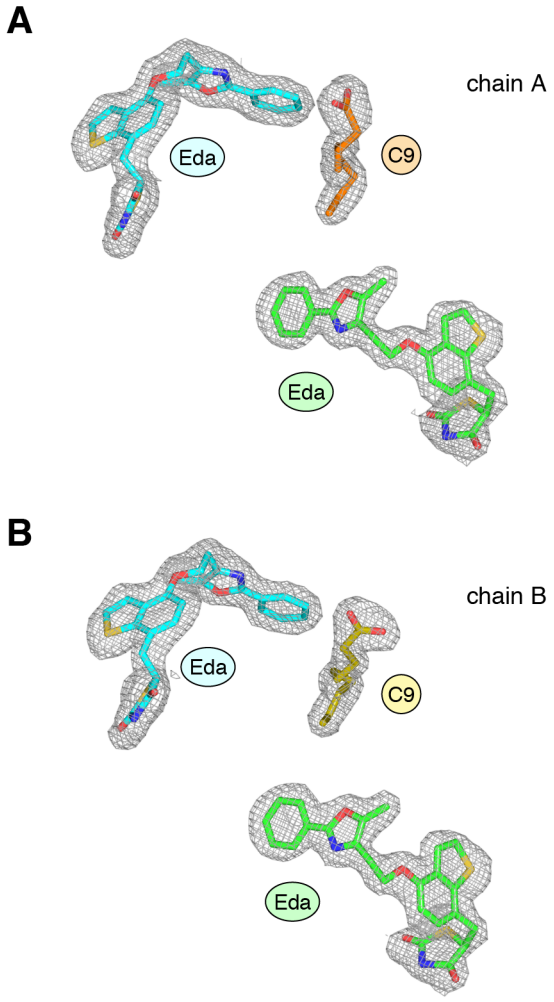

Figure S1.

Omit map (2Fo–Fc, contoured at 1 σ) of the EDA and C9 ligands in the crystal structure (PDB code 5UGM); ligands in chains A and B are shown in (**A**) and (**B**), respectively, and colored as detailed in **Figure 2**.

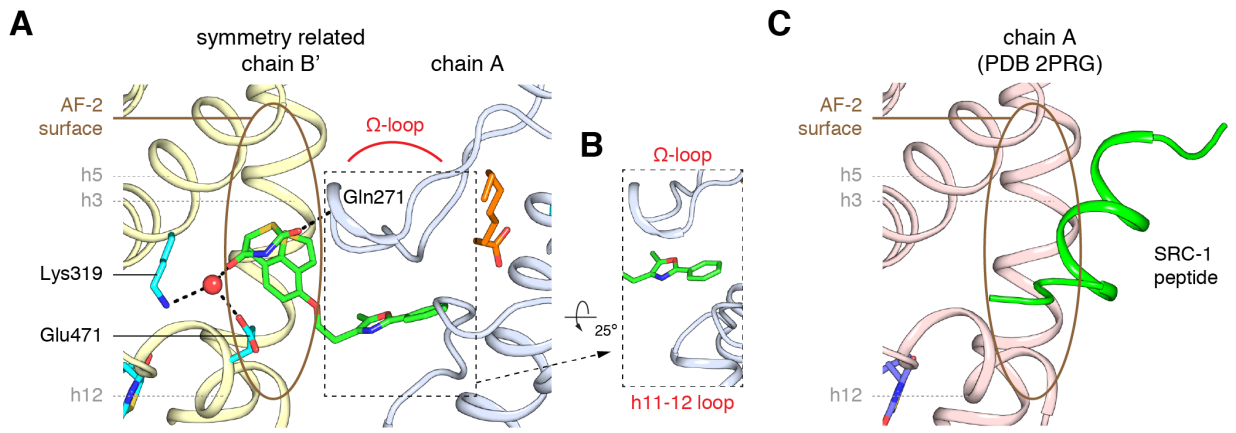

Figure S2.

The TZD head group of the second edaglitazone molecule docks into the PPARγ AF-2 surface (**A,B**) in a similar manner to a SRC-1 coactivator peptide bound to the AF-2 surface (**C**) in the crystal structure of rosiglitazone-bound PPARγ (PDB code 2PRG) (9). The hydrophobic tail group of this second edaglitazone molecule packs within a surface pocket created by the Ω-loop and the loop connecting helix 11 and 12 (**B**). The second EDA ligand bridges interactions between two PPARγ molecules in different unit cells within the crystal lattice by binding to the Ω-loop region in one molecule (e.g., chain A) and the AF-2 surface of a symmetry related molecule (e.g., chain B′).

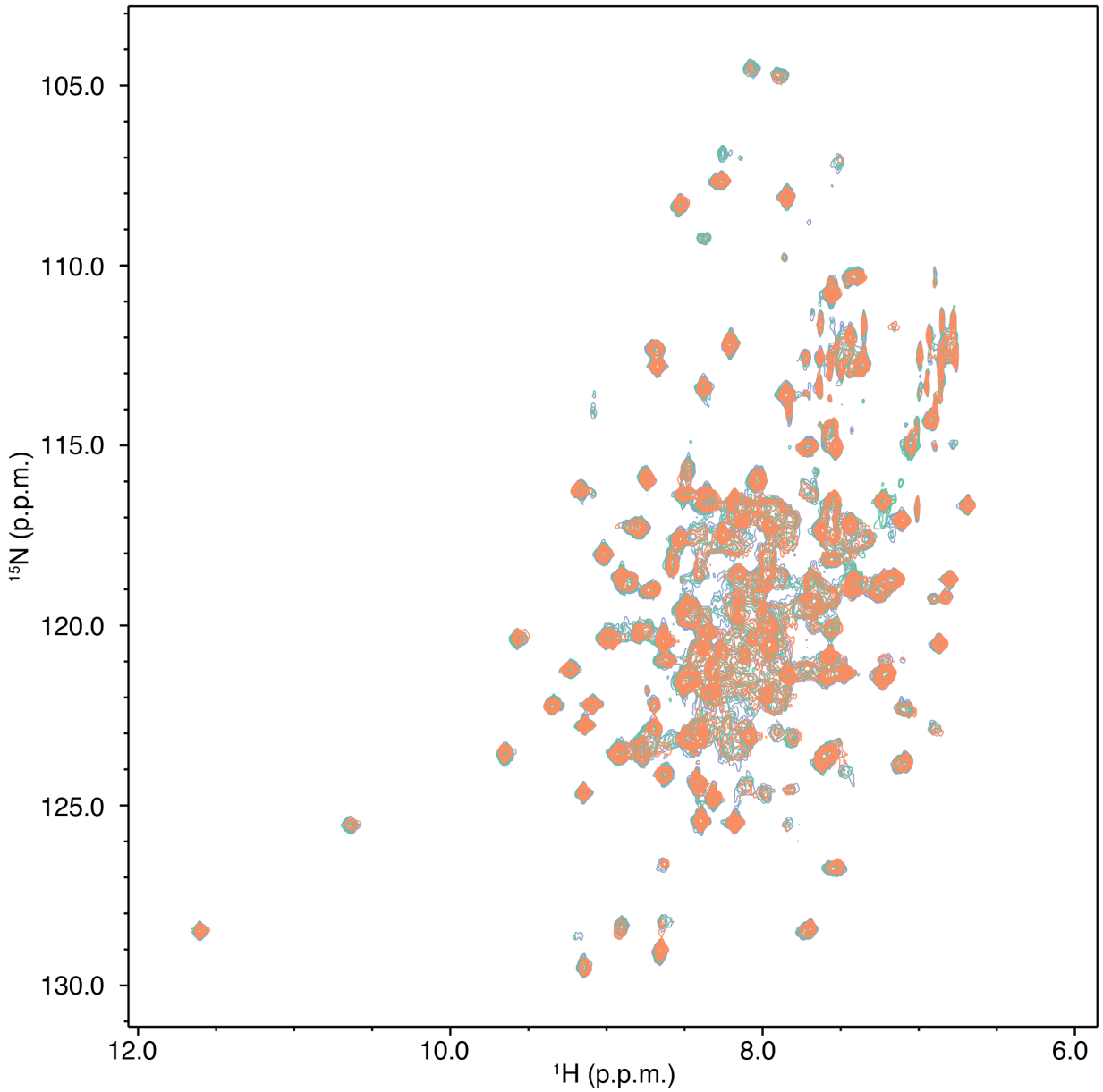

Figure S3.

Full differential 2D [^{1}H,^{15}N]-TROSY-HSQC NMR data comparing ^{15}N-labeled PPARγ LBD in the native form (red) vs. delipidated using a refolding procedure (blue) or treatment using LIPIDEX 1000 resin (green), the latter two of which are nearly identical.

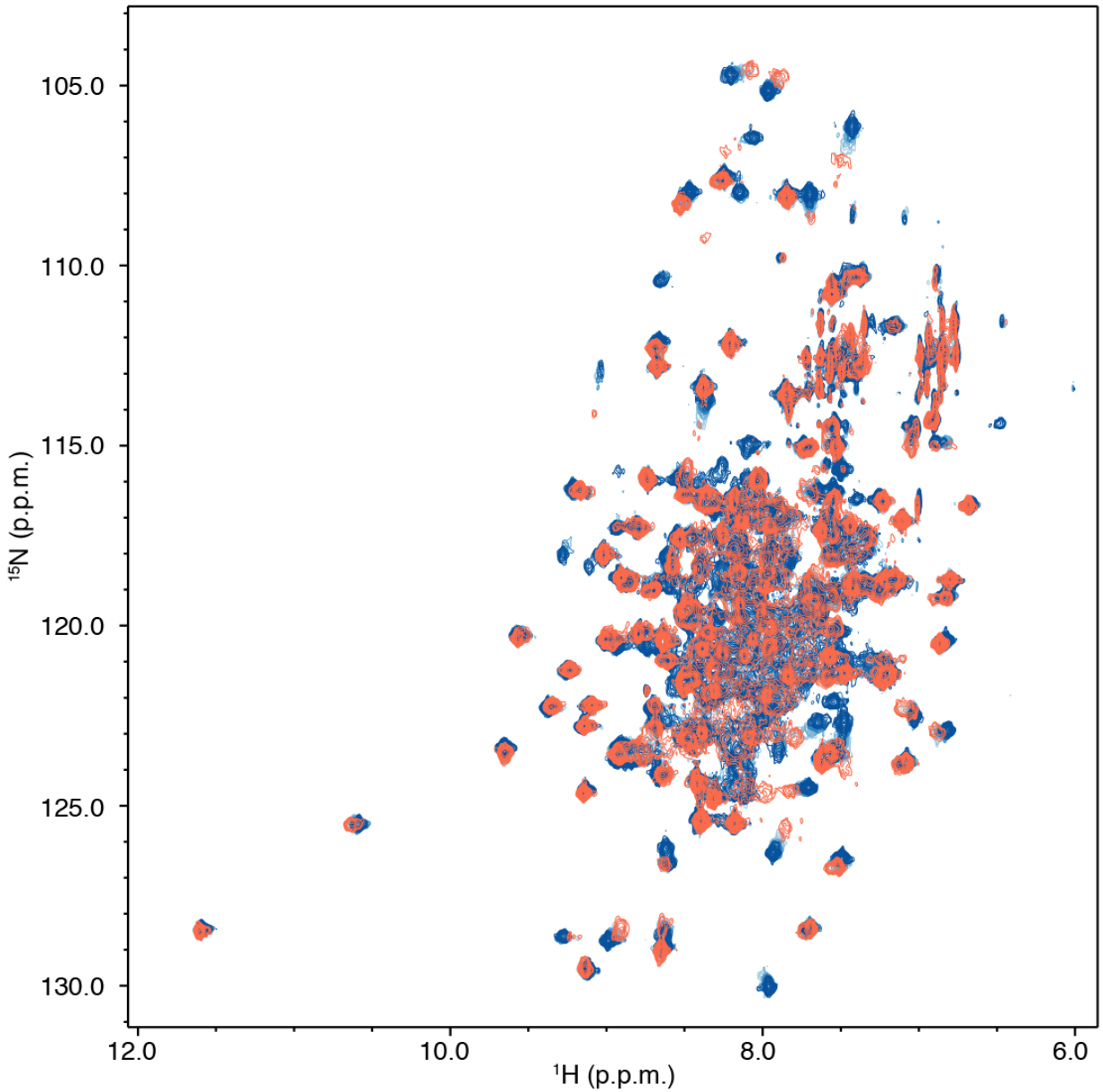

Figure S4.

Full differential 2D [^{1}H,^{15}N]-TROSY-HSQC NMR data comparing C9 (1, 2, and 3 equiv.; light, medium, and dark blue, respectively) added into native "apo" PPARγ (red).

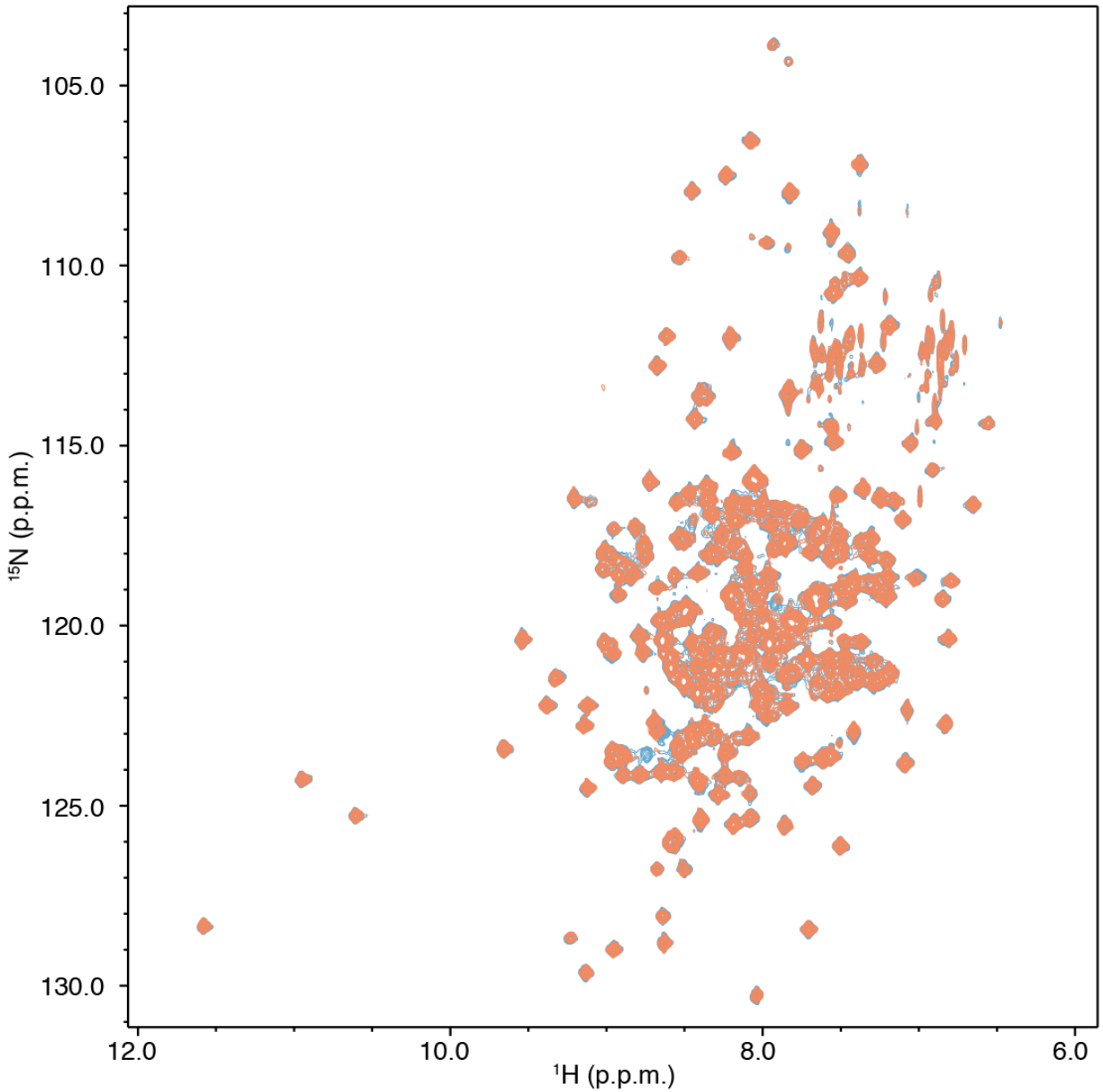

Figure S5.

Full differential 2D [^{1}H,^{15}N]-TROSY-HSQC NMR data comparing native (red) vs. delipidated (blue) PPARγ bound to rosiglitazone (2 equiv.). *Related to Figure 6A.*

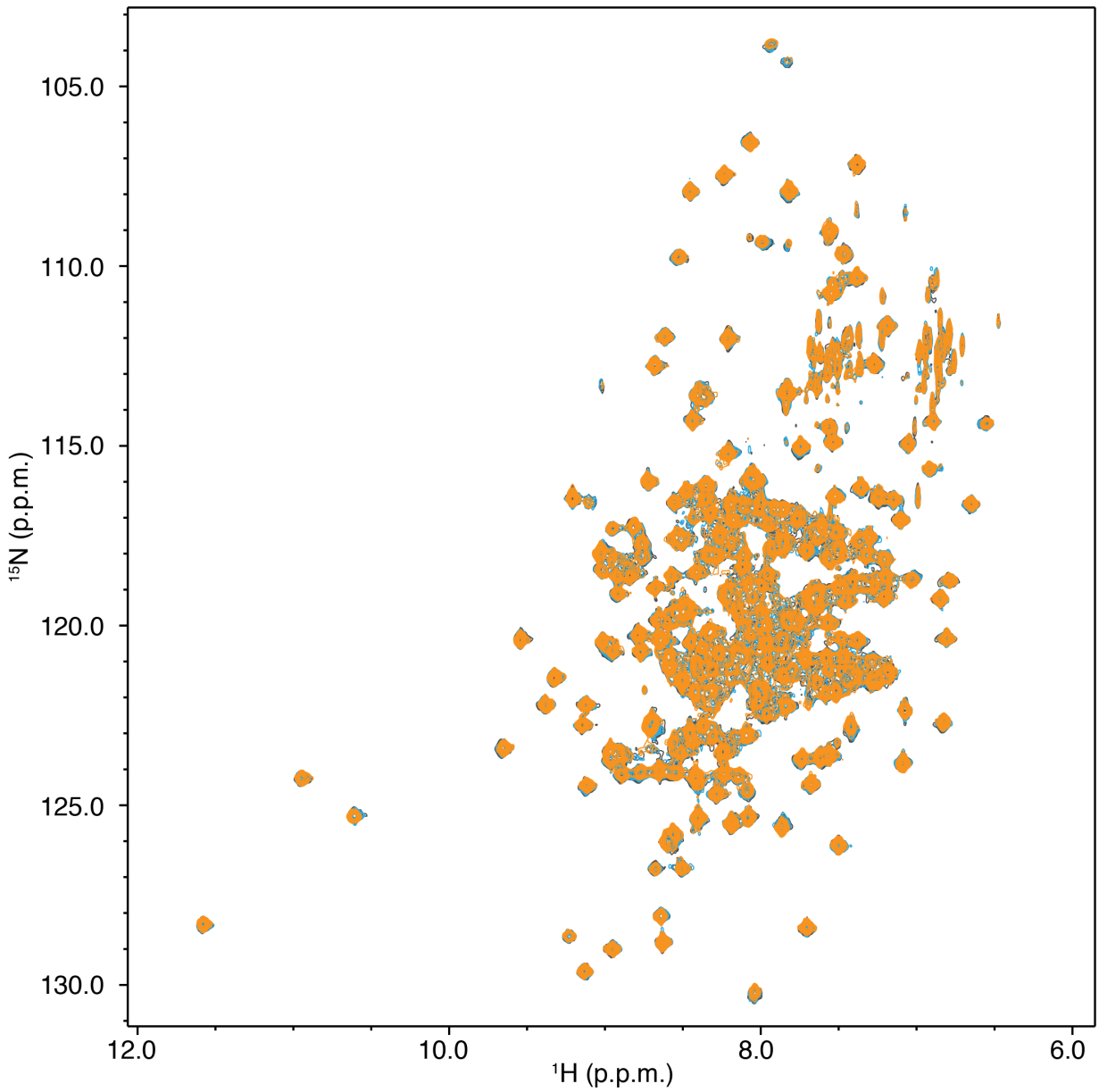

Figure S6.

Full differential 2D [^{1}H,^{15}N]-TROSY-HSQC NMR data comparing C9 (1 and 3 equiv.; blue and orange, respectively) added into native PPARγ bound to rosiglitazone (2 equiv.; black). *Related to Figure 6B.*

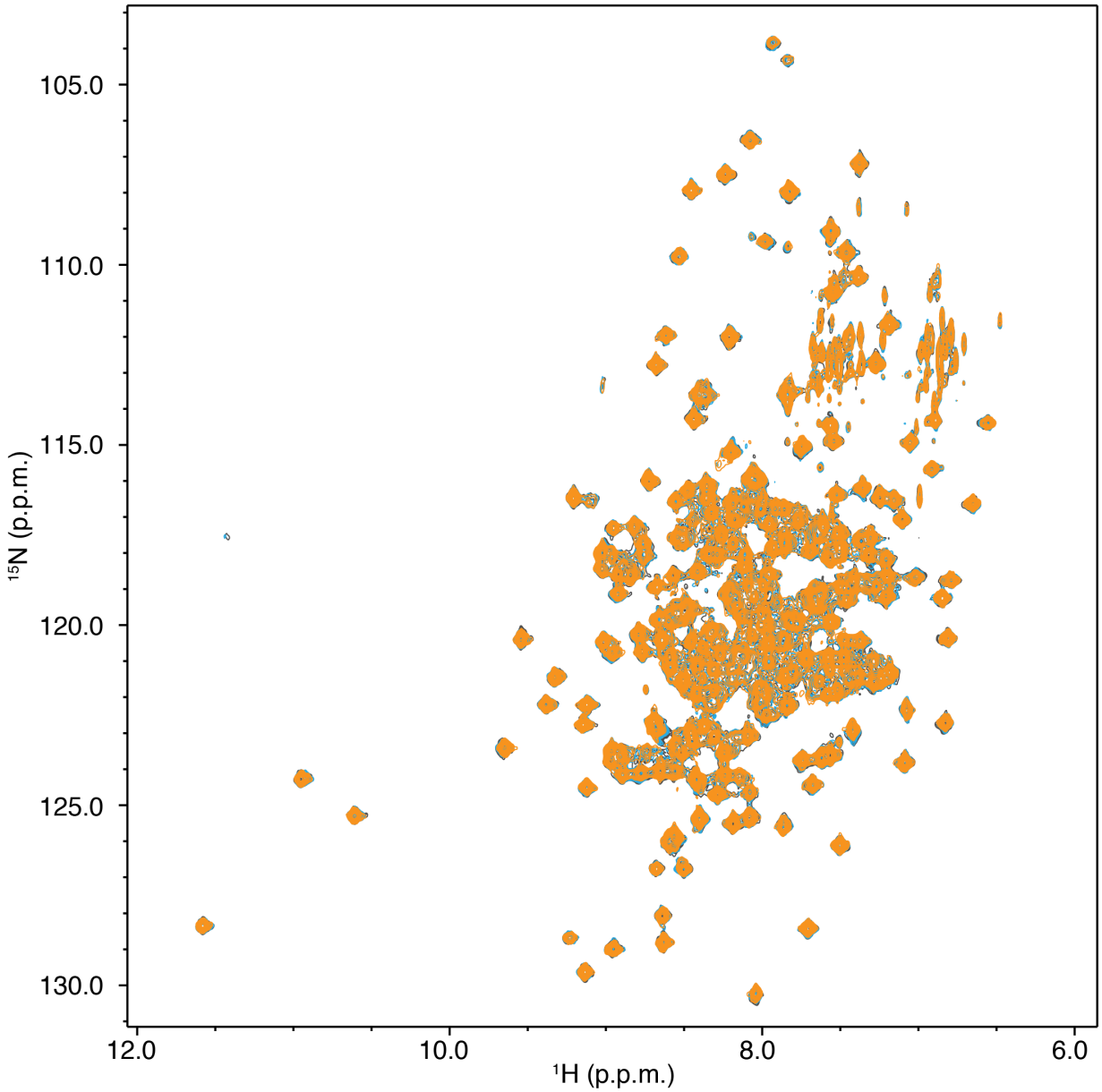

Figure S7.

Full differential 2D [^{1}H,^{15}N]-TROSY-HSQC NMR data comparing C9 (1 and 3 equiv.; blue and orange, respectively) added into delipidated PPARγ bound to rosiglitazone (2 equiv.; black). *Related to Figure 6C.*

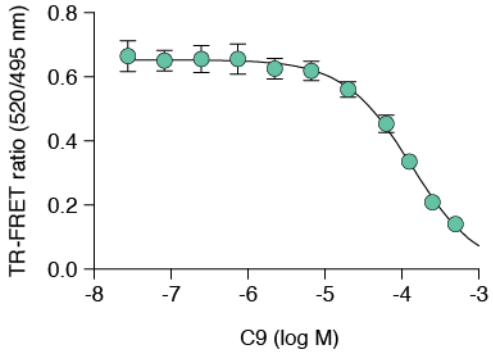

Figure S8.

TR-FRET based ligand displacement assay for C9 binding to PPARγ LBD (K_i = 47.4 μM). Data plotted as the average and S.D. of three experimental replicates.

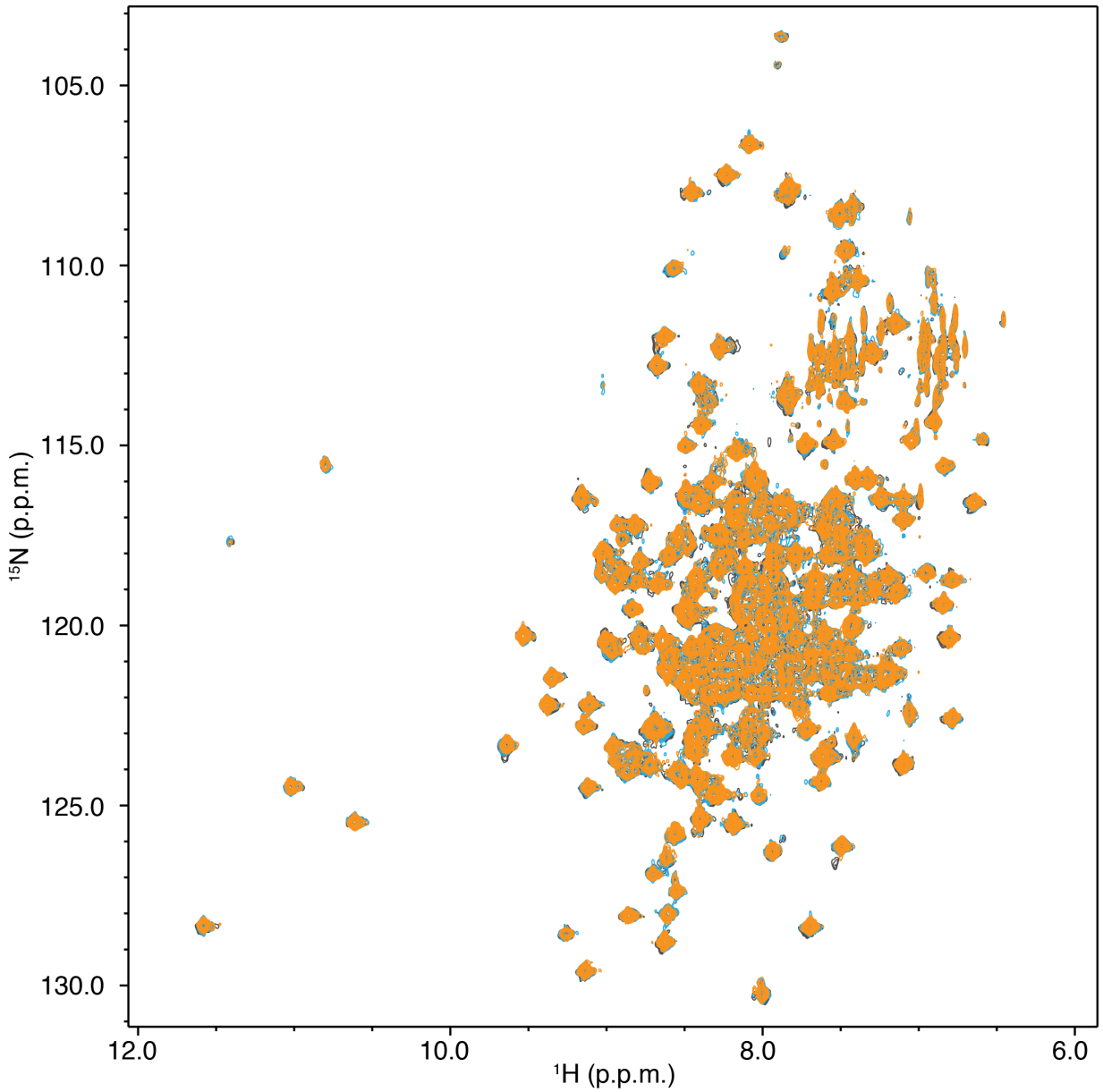

Figure S9.

Full differential 2D [^{1}H,^{15}N]-TROSY-HSQC NMR data comparing C9 (1 and 3 equiv.; blue and orange, respectively) added into native PPARγ bound to edaglitazone (2 equiv.; black). *Related to Figure 6D.*

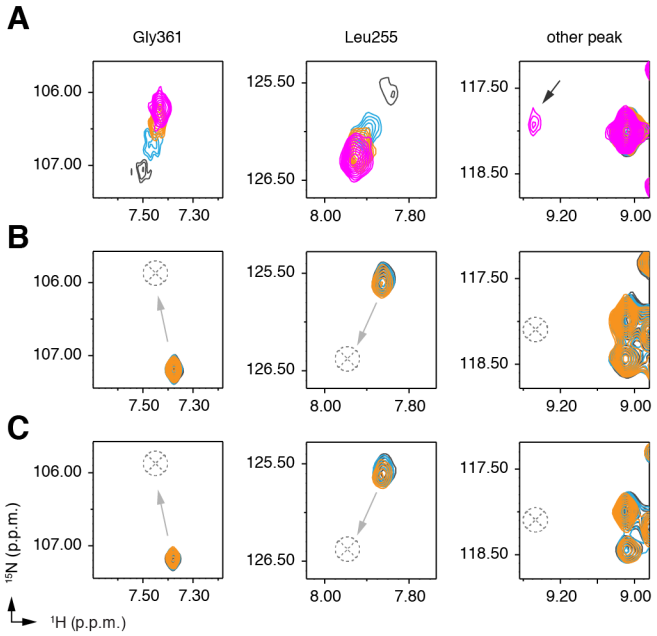

Figure S10.

Differential 2D [^{1}H,^{15}N]-TROSY-HSQC NMR data showing that chemical shifts corresponding to residues (Gly361, Leu255, and an unassigned peak) perturbed when (**A**) C9 (1, 2, and 3 equiv.; blue, orange, and magenta, respectively) binds to apo-PPARγ (black), (**B,C**) but not when C9 (1 and 3 equiv.; blue and orange, respectively) binds to rosiglitazone-bound (2 equiv.) PPARγ in the (**B**) delipidated or (**C**) native form. The black arrow denotes a peak present when PPARγ is bound to C9; grey arrows denote the lack of transition to a C9-bound peak, which is missing in the rosiglitazone-bound data (dotted circle/cross).

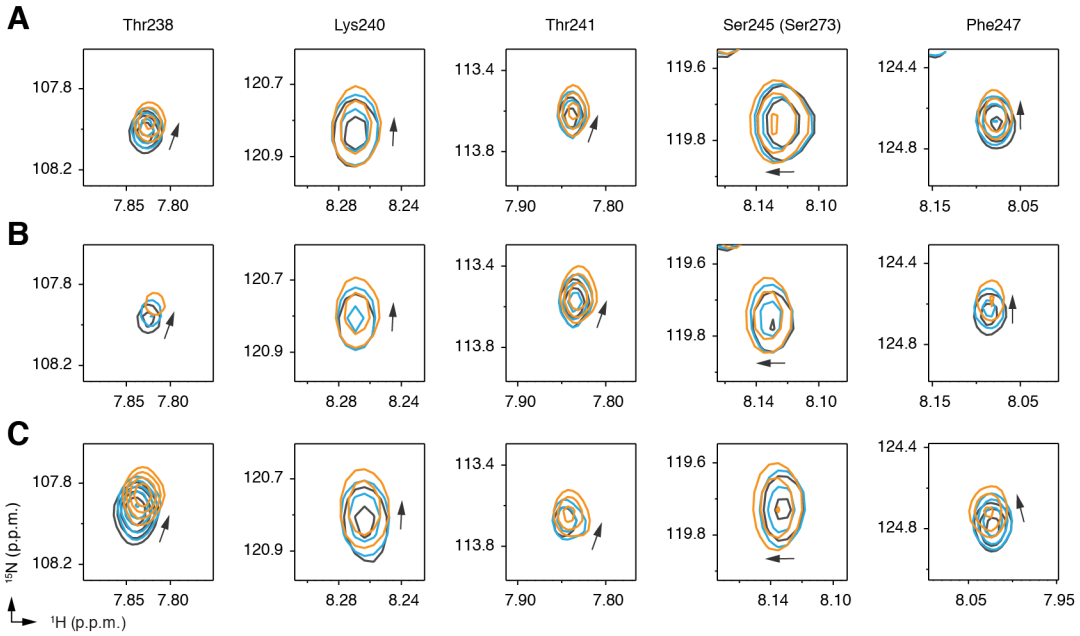

Figure S11.

Differential 2D [^{1}H,^{15}N]-TROSY-HSQC NMR data focusing on residues in the Ser273 loop comparing C9 (1 and 3 equiv.; blue and orange, respectively) added into (**A**) delipidated PPARγ bound to rosiglitazone (2 equiv.; black); (**B**) native PPARγ bound to rosiglitazone (2 equiv.; black); and (**C**) native PPARγ bound to edaglitazone (2 equiv.; black).

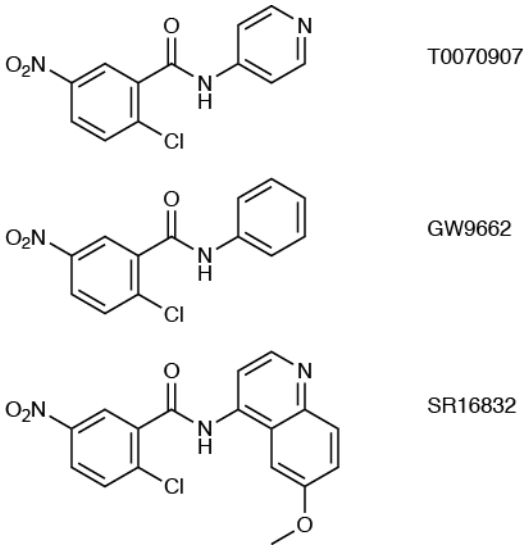

Figure S12.

Chemical structures of covalent antagonists used in this study.

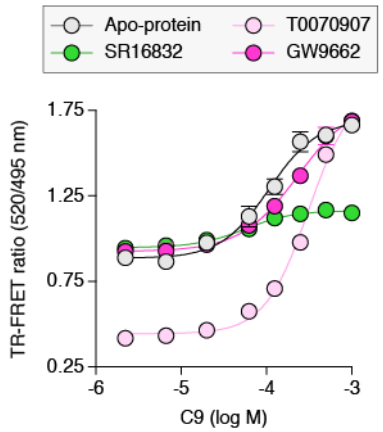

Figure S13.

TRAP220-based TR-FRET assay data (normal values; *related to normalized data in Figure 8G*). Data plotted as the average and S.D. of three experimental replicates. The differences in TR-FRET ratio values between the various conditions (apo-protein or when bound to a covalent antagonist) are a result of increased (higher values) or decreased (lower values) binding of, or affinity for, the TRAP220 coactivator peptide. Additionally, C9 cobinding to T0070907-bound PPARγ causes a larger change in affinity and thus a larger change in TR-FRET values compared to SR16832-bound PPARγ, which shows a smaller change in TR-FRET values with C9 cobinding.

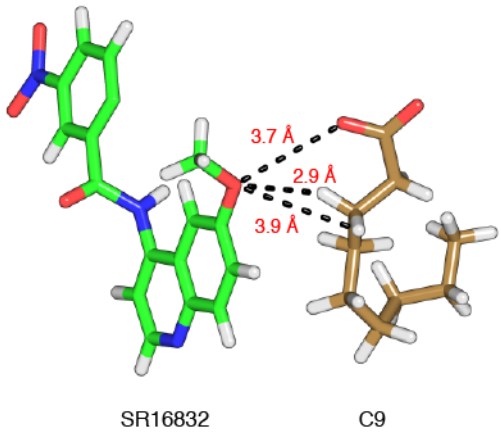

Figure S14.

Hydrogen bonds/interactions between the SR16832 methoxy group and nonanoic acid.

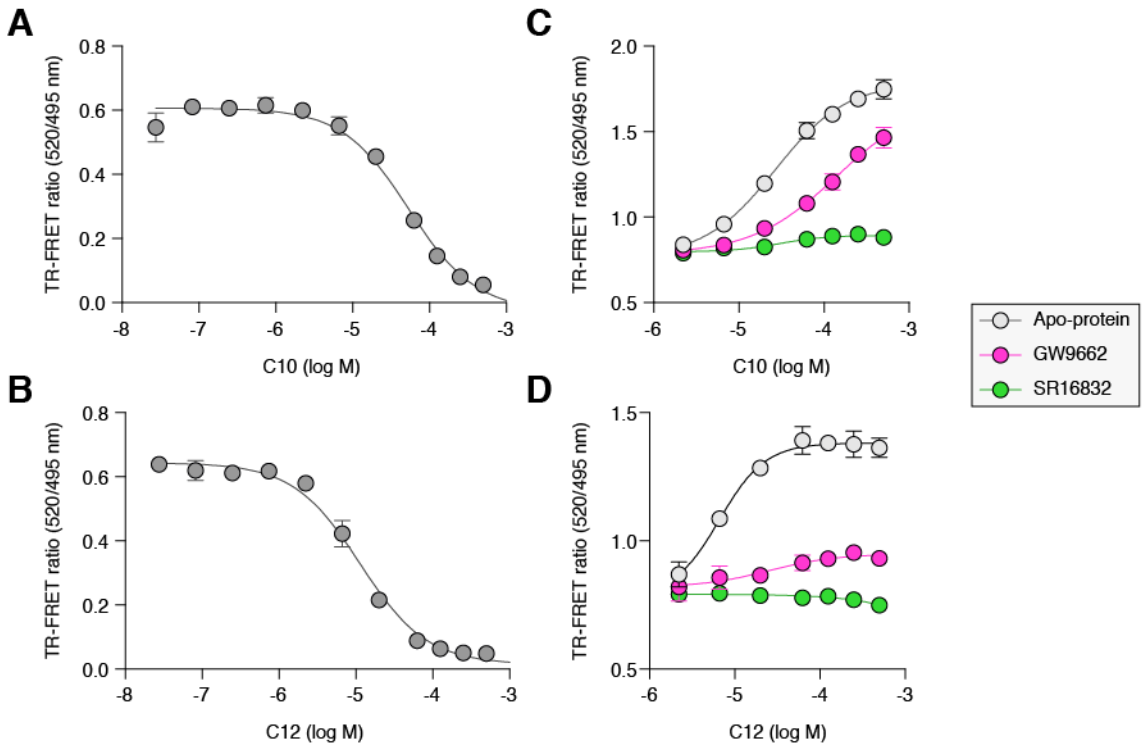

Figure S15.

(**A,B**) Ligand displacement data for decanoic acid (C10) and dodecanoic acid (C12) give K_i values of 19.4 μM and 4.1 μM, respectively. (**C,D**) TRAP220-based TR-FRET performed in the absence or presence of covalent antagonists that block orthosteric binding nonanoic acid ligands to various degrees. Data plotted as the average and S.D. of three experimental replicates.

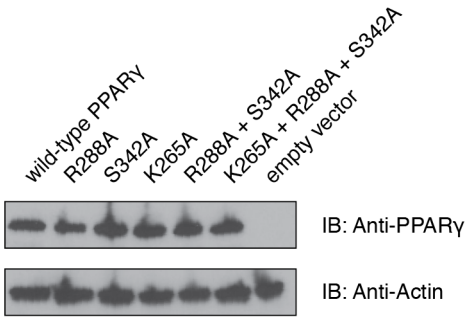

Figure S16.

Western blot analysis protein levels in HEK293T cells transfected with wild-type or mutant full-length PPARγ expression plasmids.

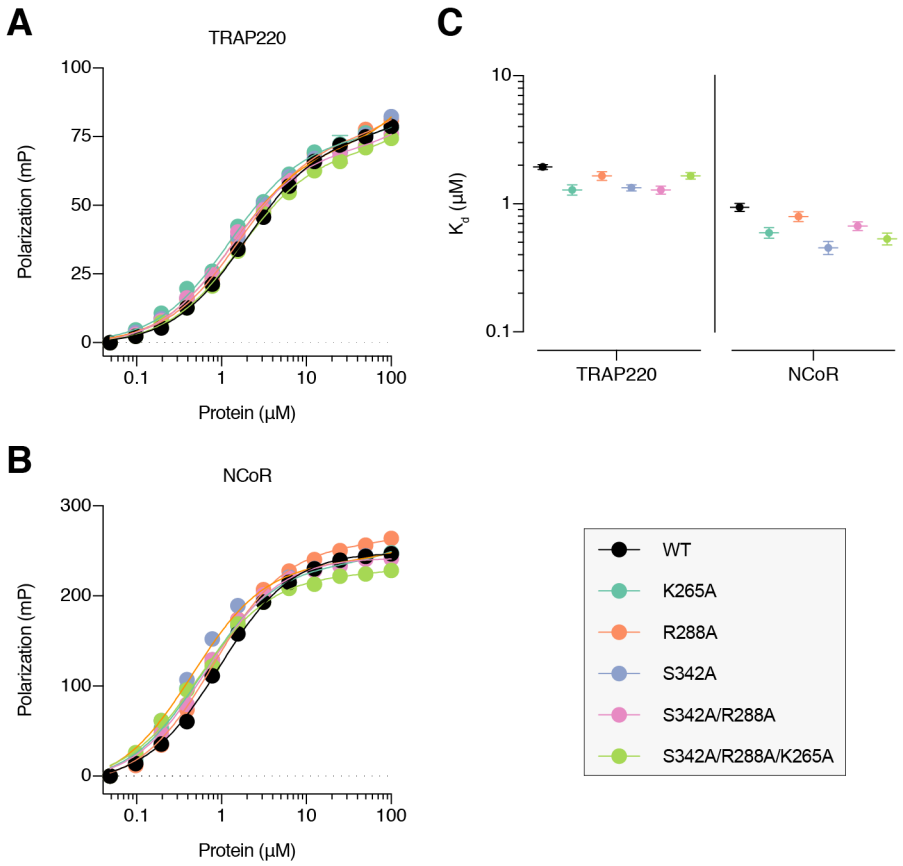

Figure S17.

Fluorescence polarization (FP) assays performed using wild-type and mutant PPARγ LBD protein with FITC-labeled peptides derived from (**A**) TRAP220 coactivator and (**B**) NCoR corepressor shows (**C**) similar affinities. Data in (**A,B**) plotted as the average and S.D. of three experimental replicates; data in (**C**) show the K_d values and fitted errors for the data in (**A,B**) that were fitted to a one site total binding equation.

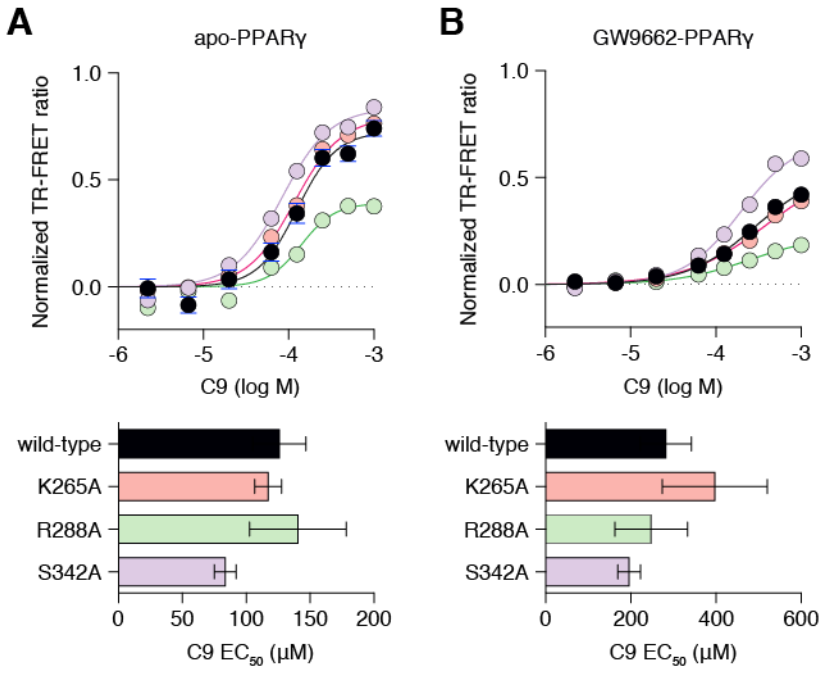

Figure S18.

TR-FRET assays performed using wild-type and mutant PPARγ LBD protein in the (**A**) absence or (**B**) presence of GW9662 involved in hydrogen bonds with nonanoic acid shows similar EC_{50} values for nonanoic acid. Data plotted as the average and S.D. of three experimental replicates.

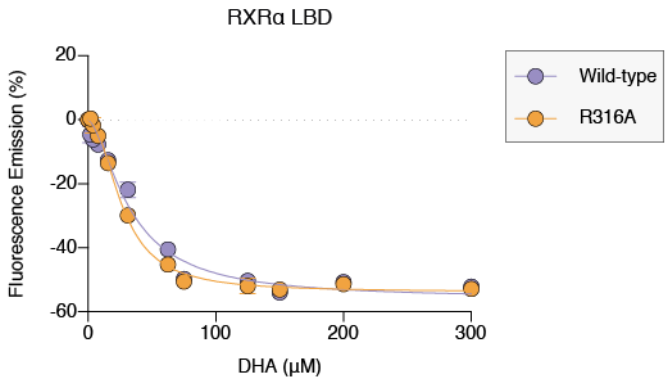

Figure S19.

Tryptophan fluorescence binding assays performed using wild-type (33.2 ± 4.9 μM) or R316A mutant (28.6 ± 1.0 μM) RXRα LBD protein. Data plotted as the average and S.E.M. of two experimental replicates.

Table 1. X-ray data collection and refinement statistics

	PPARγ + edaglitazone and nonanoic acid
Data collection	APS-LS-CAT-21-ID-D
Space group	I4
Cell dimensions	
a, *b*, *c* (Å)	128.74, 128.74, 93.67
α, *β*, *γ* (°)	90, 90, 90
Resolution	33.36 – 2.1 (2.175 – 2.1)
R_{pim}	0.05 (0.299)
I / σ(I)	9.87 (2.83)
*CC*1/2 in highest shell	0.798
Completeness (%)	99.31 (99.69)
Redundancy	2.0
Refinement	
Resolution (Å)	2.1
No. of reflections	87972
R_{work}/R_{free} (%)	18.2/21.6
No. of atoms	
Protein	4354
Water	473
B-factors	
Protein	27.3
Ligand	29.14
Water	33.73
Root mean square deviations	
Bond lengths (Å)	0.008
Bond angles (°)	1.18
Ramachandran favored (%)	96.28
Ramachandran outliers (%)	0.93
PDB accession code	5UGM
Values in parentheses indicate highest resolution shell.	

Table 2. X-ray data collection and refinement statistics

	PPARγ LBD + GW9662 and nonanoic acid	PPARγ LBD + SR16832 and nonanoic acid
Data collection	BCSB-5.0.2	MicroMax007 HF
Space group	C 1 2 1	C 1 2 1
Cell dimensions		
a, *b*, *c* (Å)	92.61, 62.08, 118.45	92.57, 61.74, 118.38
α, *β*, *γ* (°)	90, 102.34, 90	90, 102.15, 90
Resolution	45.24 – 2.73 (2.828 – 2.73)	57.86 – 2.29 (2.372 – 2.29)
R_{pim}	0.04 (0.338)	0.03 (0.613)
I / σ(I)	10.43 (2.00)	11.90 (1.33)
*CC*1/2 in highest shell	0.832	0.757
Completeness (%)	85.06 (74.34)	98.94 (98.00)
Redundancy	1.8	6.6
Refinement		
Resolution (Å)	2.73	2.29
No. of reflections	26613	29660
R_{work}/R_{free} (%)	19.9/28.1	24.9/31.4
No. of atoms		
Protein	4187	4145
Water	60	243
B-factors		
Protein	30.29	33.77
Ligand	39.84	45.19
Water	21.44	30.89
Root mean square deviations		
Bond lengths (Å)	0.009	0.009
Bond angles (°)	1.09	1.02
Ramachandran favored (%)	90.43	95.27
Ramachandran outliers (%)	1.95	1.58
PDB accession code	6AUG	6AVI
Values in parentheses indicate highest resolution shell.		